The International Journal of Advanced Manufacturing Technology (2025) 141:4505–4525
https://doi.org/10.1007/s00170-025-16691-5

ORIGINAL ARTICLE

Grinding-assisted electrochemical discharge machining of ZrO_2 ceramics with constant force feed control

Zhijian Huang[1,2] · **Zhixiang Zou**[1] · **Zhiming Wu**[2] · **Kangcheung Chan**[1] · **Jiangwen Liu**[2]

Received: 21 June 2025 / Accepted: 25 September 2025 / Published online: 13 November 2025

Abstract

Grinding-assisted electrochemical discharge machining (G-ECDM) shows great potential for efficient and high-precision machining of insulating hard and brittle materials such as glass. However, research on ZrO_2 ceramics, which have higher melting points and lower thermal conductivity, is still relatively lacking. To expand the application range of G-ECDM and address the thermal defects that occur in ZrO_2 ceramics in conventional ECDM, this paper proposes a G-ECDM method based on constant spring force feedback feed. This approach aims to achieve faster removal of material affected by discharge heat through the grinding action of the abrasives, thereby avoiding excessive heat accumulation inside the material, and reducing the generation of thermally induced cracks with larger overcut. The feed force can be effectively controlled by means of a constant spring force feed, enabling better conditions for the synergistic action of grinding and discharging and preventing damage to the tool electrodes. In addition, previous research on G-ECDM has primarily focused on the grinding effect of abrasive tools, with few studies addressing the effects of the process on gas film formation and discharge. Therefore, this paper also investigates the impact of abrasive electrodes on gas film formation and discharge properties, while also examining the removal mechanism of ZrO_2 ceramics during G-ECDM. Through a series of process parameter optimizations, high-quality small hole machining of ZrO_2 ceramics was successfully achieved. This research provides an important basis for improving the theory of the G-ECDM process and expanding its application in high-temperature engineering ceramics.

Keywords Electrochemical discharge machining (ECDM) · ZrO_2 ceramics · Abrasive electrode · Constant force feed · Small hole machining

1 Introduction

ZrO_2 ceramics are widely used in defense [1], electronics, aerospace [2], and clinical medicine [3] applications owing to their excellent physicochemical properties such as high hardness, corrosion resistance, chemical stability, low thermal conductivity, and high dielectric constant. In practical application scenarios, these parts made of ZrO_2 ceramics often require the machining of structures such as small holes and microchannels. Examples include the machining of film-cooling holes in the YSZ thermal barrier coating of gas turbine hot section components [4] and small holes in ceramic substrates for mounting pins for electronic components [5]. These structures are difficult to achieve directly on ceramic parts using conventional ceramic pressing and sintering processes [6]. Nevertheless, the hard and brittle nature of ZrO_2 ceramics makes conventional machining processes prone to serious tool wear and workpiece damage [7]. To meet the demand for engineering applications of ZrO_2 ceramics, non-traditional machining methods such as ultrasonic machining [8], laser machining [9], abrasive water jet machining [10], and electrical discharge machining (EDM) [11] have also been employed in the fabrication of ZrO_2 ceramic components. However, these methods present

✉ Kangcheung Chan
kc.chan@polyu.edu.hk

✉ Jiangwen Liu
fejwliu@scut.edu.cn

Zhixiang Zou
zouzx606@163.com

[1] Department of Industrial and Systems Engineering, Research Institute for Advanced Manufacturing, The Hong Kong Polytechnic University, Hung Hom, Hong Kong, People's Republic of China

[2] State Key Laboratory of Precision Electronic Manufacturing Technology and Equipment, Guangdong University of Technology, Guangzhou 51006, People's Republic of China

critical challenges such as severe tool wear, low dimensional accuracy, high equipment costs, and thermal damage [6]. Among them, EDM is relatively economical and fast, but it requires the workpiece material to be electrically conductive (conductivity value > 0.01 S/cm), making it difficult to apply directly to insulating ceramics such as ZrO_2 [12]. Although the EDM with assisting electrode (EDM-AE) method proposed by Mohri and Fukuzawa [13] can address the issue of material conductivity, the conductive film on the surface of the area to be machined does not form stably during the actual machining process, thus failing to maintain a stable and continuous discharge [12]. It has also been reported that using larger discharge parameters can induce the generation of conductive films, but at the same time, it also brings significant thermal impact problems, leading to thermal damage [14]. In contrast, electrochemical discharge machining (ECDM) relies on the continuous formation of a gas film generated by electrolysis to initiate spark discharges. This gas film formation is more stable than the conductive film formation in EDM-AE, thereby providing more stable discharge conditions. In addition, due to its flexibility, simplicity, low cost, and minimal structural damage, researchers consider it to have great potential for processing insulating hard and brittle materials, including ceramics and glass [15].

In ECDM, the gap between the workpiece material and the tool electrode is known as the working gap [16]. During the material removal process, the size of the working gap directly determines the effective utilization of electrochemical discharge energy [17]. Arab et al. [18] also noted that within the critical working gap, a larger working gap causes the machined surface to become rougher, while a smaller gap increases tool electrode wear. To better control the working gap, researchers have developed various feed strategies including constant velocity feed, gravity feed, and force feedback feed [19]. When machining with constant velocity feed, to avoid damage to the workpiece or tool electrode, the feed rate should be less than or equal to the material removal rate (MRR) during the machining process [20]. However, in the actual machining process, the MRR changes with the machining depth, and it is difficult to monitor the change of the working gap in real time. Ziki and Wüthrich [21] investigated the variation of force applied to the tool during ECDM drilling for different voltages, electrode sizes, and feed rates, and indicated the possibility of using force as a feedback signal to monitor the ECDM process. The gravity feed method with almost zero working gap is one of the more popular feeding strategies in recent years [20]. However. the contact forces generated during machining expose tool electrodes, especially microtools, to the risk of bending and fracture [22]. To avoid electrode bending due to excessive contact force during Micro-ECDM, Nawaz et al. [23] developed a spindle with flexible force feedback to maintain a stable micro-contact force between the tool electrode and the workpiece. They also compared the machining performance of the gravity feed method and the spring-force feedback feed method for machining microstructures such as blind holes and channels in quartz glass. The results showed that the latter was able to reduce electrode deflection and achieve higher machining accuracy [24]. Singh and Dvivedi [25] reported a pressurized feeding system and fabricated micro holes with a depth of up to 1537 μm in borosilicate glass using a tool electrode coated with SiC abrasives. They noted that under pressurized feed, the abrasives provided tiny cavities between the tool electrode and the workpiece, thus formed thinner gas films and generated high frequency and low intensity discharges.

The use of abrasive tool electrodes also introduces a mechanical grinding action further improving material removal efficiency and machining quality. Jain et al. [26] compared the machining efficiency of ECDM and grinding assisted electrochemical discharge machining (G-ECDM) on borosilicate glass and alumina ceramics. Their experimental results demonstrated that grinding tools enhance material removal and increase the depth of machining. Wang et al. [27] compared the machining performance of conventional ECDM and G-ECDM in glass microchannels, and pointed out that G-ECDM can effectively eliminate the heat-affected zone and thermally induced defects generated by discharge, reducing overcutting by 49.1% and edge damage by 56.6%. Laddesh and Manu [28] used the ratio of the tool feed rate to the depth of the thermally softened layer of the material to predict the relative contribution of electrochemical discharge action and grinding action to material removal in G-ECDM. The G-ECDM experiments on soda lime silica glass also verified that when the grinding action and the thermo-melting action of the discharge are in equilibrium, it is possible to effectively remove and thermally soften the material and recast layer by the grinding action of the abrasive tool.

In the past, research on ECDM has mainly focused on glass materials, with relatively few studies on insulating engineering ceramics such as ZrO_2. Compared to glass, engineering ceramics not only have higher melting points, but also lower thermal conductivity. While the use of greater discharge energy can improve its machining efficiency, it also tends to exacerbate the formation of thermally induced cracks, making it difficult to ensure machining quality. The G-ECDM methods mentioned above have been proven to improve machining quality and efficiency on materials such as glass, alumina ceramics, etc. by removing material softened or melted by electrochemical discharges with abrasive grains. However, it should be noted that in materials such as glass, as well as Si_3N_4, Al_2O_3, their intergranular glass phase can soften at high temperature, while ZrO_2 ceramics have very few intergranular glass phase [29]. Therefore, there is no thermal softening in G-ECDM for ZrO_2 ceramics. However, there are relatively few studies in G-ECDM

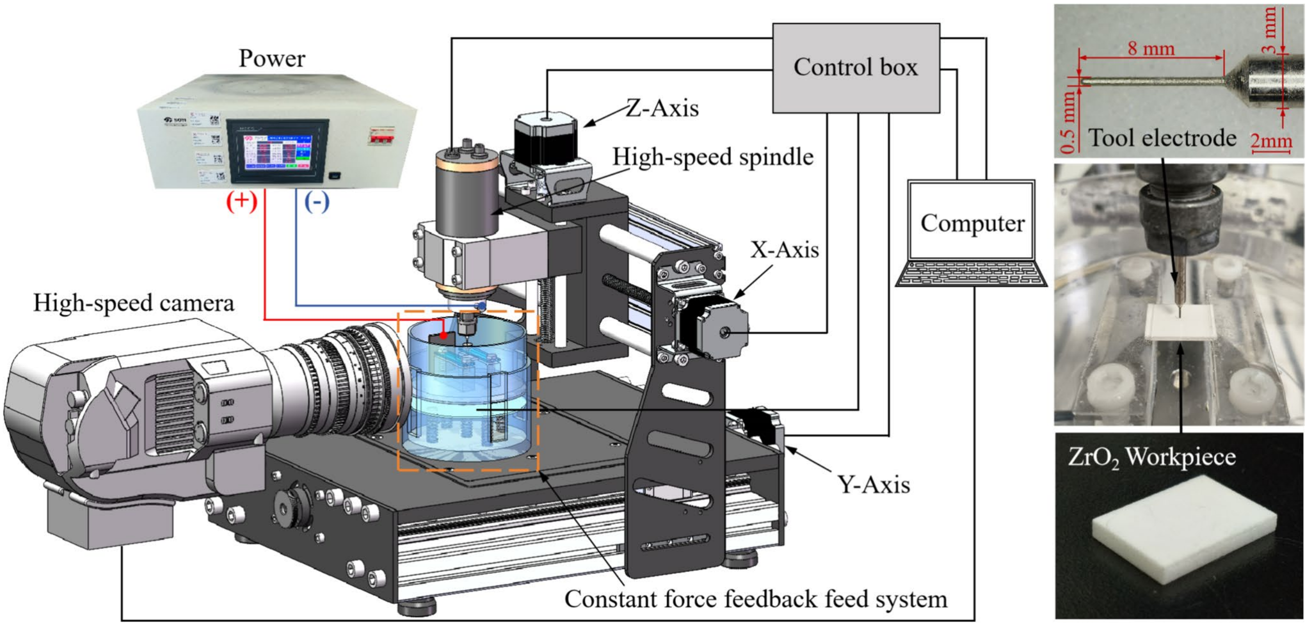

Fig. 1 Schematic diagram of the G-ECDM experimental setup

for ZrO_2 ceramics, and the material removal mechanism is not yet clear.

Based on previous research, this paper proposes a high-speed grinding-assisted electrochemical discharge machining method with constant spring force feedback feed to solve the problems of poor machining quality and low machining accuracy of ZrO_2 ceramics caused by high temperature thermal shock of the discharge in the traditional ECDM process. In this study, the machining of small holes in ZrO_2 ceramics is investigated. Three main aspects of the process, namely the electrochemical discharge characteristics, the material removal mechanism, and the influence of process parameters, are investigated to demonstrate the potential application of this method in ZrO_2 ceramics processing.

2 Experimental setup and methods

2.1 Experimental setup

All machining experiments in this study were performed on a self-built ECDM platform. Figure 1 shows the G-ECDM platform consisting of a pulse power supply (SOYI-12020DM, Shanghai Soyi., China), a high-speed camera (FASTACM SA-Z&200K-M-8Gb, Photron, Japan), a motion controller unit, a three-dimensional motion platform, and a constant spring force feedback feed system. The tool electrode was mounted on a high-speed rotating spindle (speed range 0–40,000 rpm). The ZrO_2 workpiece and the auxiliary electrode were fixed in the electrolyte tank and were in a fully submerged state during processing. This study selected electroplated PCD abrasive tools as tool electrodes, with SKD11 steel as the tool substrate material. In this study, both conventional electrodes and abrasive electrodes after electroplating had a diameter of 500 µm. By measuring the height variation in the radial cross-section of the abrasive electrode, the protrusion height of the abrasive particles was found to range from 2/5 to 2/3 of their particle diameter. The relevant experimental conditions are detailed in Table 1.

2.2 Constant force feedback feed system

As shown in Fig. 2, a pressure sensor installed between the uniformly distributed compression spring and the electrolyte tank is used to detect the feed force (contact force between the workpiece and the tool electrode). A data acquisition card collects the voltage signal corresponding to the feed force and outputs it to the motion control system. The motion control system converts the input voltage signal into

Table 1 Experimental conditions for G-ECDM of ZrO_2

Parameter	Value
Tool electrode (cathode)	Φ500 µm, SKD11 Steel coated with PCD abrasive
Workpiece	14*19*2.5 mm ZrO_2 ceramic plate
Auxiliary electrode (anode)	40*30*3 mm Graphite
Electrolyte	15 wt% KOH
Inter-electrode gap	50 mm
Immersion depth	2 mm

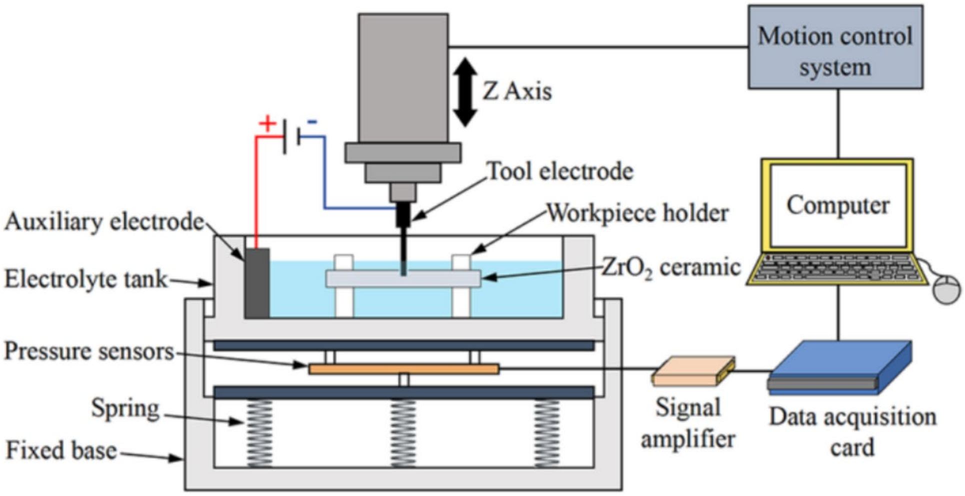

Fig. 2 Schematics diagram of constant spring force feedback control feed system

actual contact force and controls the motion of the Z-axis according to the magnitude of the actual contact force. To avoid the shaking of the up and down movable electrolyte bath in the horizontal direction during the machining process, it is necessary to maintain a high fit precision between the electrolyte bath and the fixed base, as well as to ensure very low friction resistance between their contact surfaces.

The spring feed force feedback motion control process is shown in Fig. 3. When the tool electrode is not in contact with the workpiece, the pressure sensor is subjected to the pressure of the electrolyte and the weight of the electrolyte tank, among other factors. It is necessary to zero the pressure value output by the sensor and set the desired feed force F_e. As the Z-axis begins to feed downwards, machining starts once the output force value reaches the set feed force F_e, the machining starts. During each feed force sampling cycle, the system compares the real-time feed force F_f with the set value and executes different motion control actions for the Z-axis. If the real-time feed force is less than the set value, the Z-axis will continue feeding and enter the next sampling cycle. If the feed force exceeds the set value, the Z-axis will quickly retract and enter the next sampling cycle. When the real-time feed force equals the set value, the system determines that constant-force feed has been achieved. The Z-axis will pause its movement and enter the next sampling cycle. Once the preset machining time is reached, the feed force feedback motion control process will also cease.

2.3 Experiment design

In this study, firstly, an experimental comparison was conducted to preliminarily examine the surface characteristics differences between ZrO_2 ceramic small hole machining via ECDM and G-ECDM, demonstrating the advantages of G-ECDM. Additionally, a series of experiments were conducted on the electrical discharge drilling process of ZrO_2 ceramics to investigate the effects of pulse voltage, abrasive size, feed force, and rotation speed on small hole machining performance. The relevant experimental parameters are listed in Table 2. Furthermore, through central composite design (CCD) experiments and utilizing response surface methodology, an optimal combination was obtained. Before the experiment, the ZrO_2 workpiece and tool electrodes were ultrasonically cleaned with anhydrous ethanol for 5 min. To avoid the effect of tool wear on the test results, the tool was replaced after each individual test. Each experiment was repeated five times and the average value was used as the final response.

2.4 Measurement and characterization

A scanning electron microscope (SEM, S3400N, Hitachi, Japan) was used to analyze the surface morphology of small holes and tools, while an energy dispersive X-ray spectrometer (EDS, Bruker) was used to analyze the chemical composition of their surfaces. Three-dimensional images of the small holes were obtained using a laser confocal scanning microscope (LCSM, OLS4000, Olympus, Japan), and the LEXT analysis application software was used to measure the three-dimensional contours of the small holes. Hole depth, hole overcut (HOC), and heat-affected zone (HAZ) are typically used to measure machining efficiency, machining accuracy, and machining quality, respectively [30]. This study also employs these three metrics as the primary basis for evaluating machining performance. The contour profile of the small hole was obtained by LCSM. The

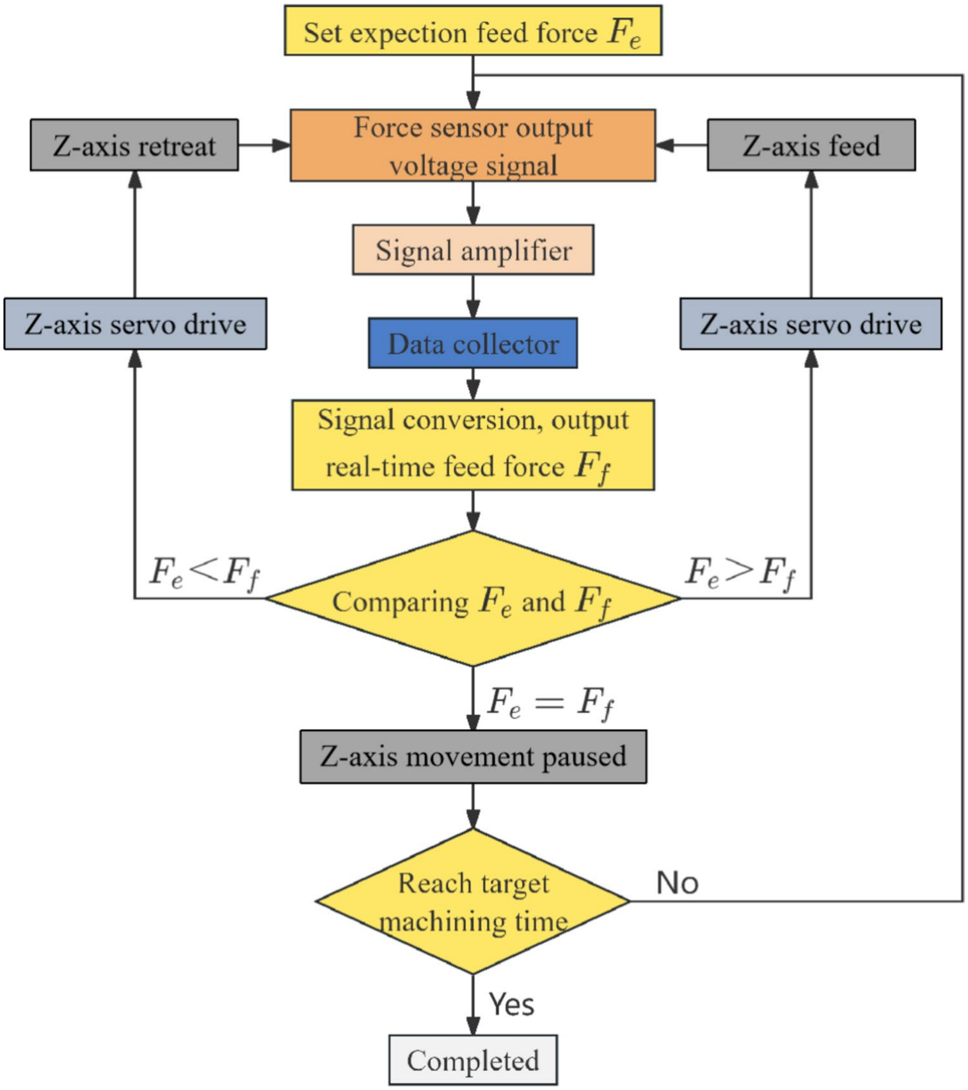

Fig. 3 Feed force feedback motion control process

measurement of the small hole parameters is shown in Fig. 4. The HOC is defined as half the difference between the hole entrance diameter D_{ent} and the tool electrode diameter R_t (Eq. 1).

$$HOC = \frac{D_{ent} - R_t}{2} \quad (1)$$

Table 2 Parameters used in the G-ECDM experiments

G-ECDM Parameters	Value
Pulse voltage (V)	45, 50, 55, 60
Pulse frequency (kHz)	10, 15
Pulse duty cycle (%)	80
Rotation speed (rpm)	6000
Abrasive grains size	200, 400, 600, 800-mesh
Feed force (N)	1, 3, 5, 7, 9, 11, 13, 15

3 Effect of electrode type on gas film formation

The gas film around the surface of the tool electrode is essential for electrochemical discharge, and the stability and thickness of the gas film determine the quality and precision of the small holes machined. To investigate the effect of abrasive electrodes on bubble growth and gas film formation, we used a high-speed camera to capture and analyze the bubble generation and gas film formation of both conventional and abrasive electrodes in real time. In this experiment, a conventional cylindrical electrode, 200-mesh and

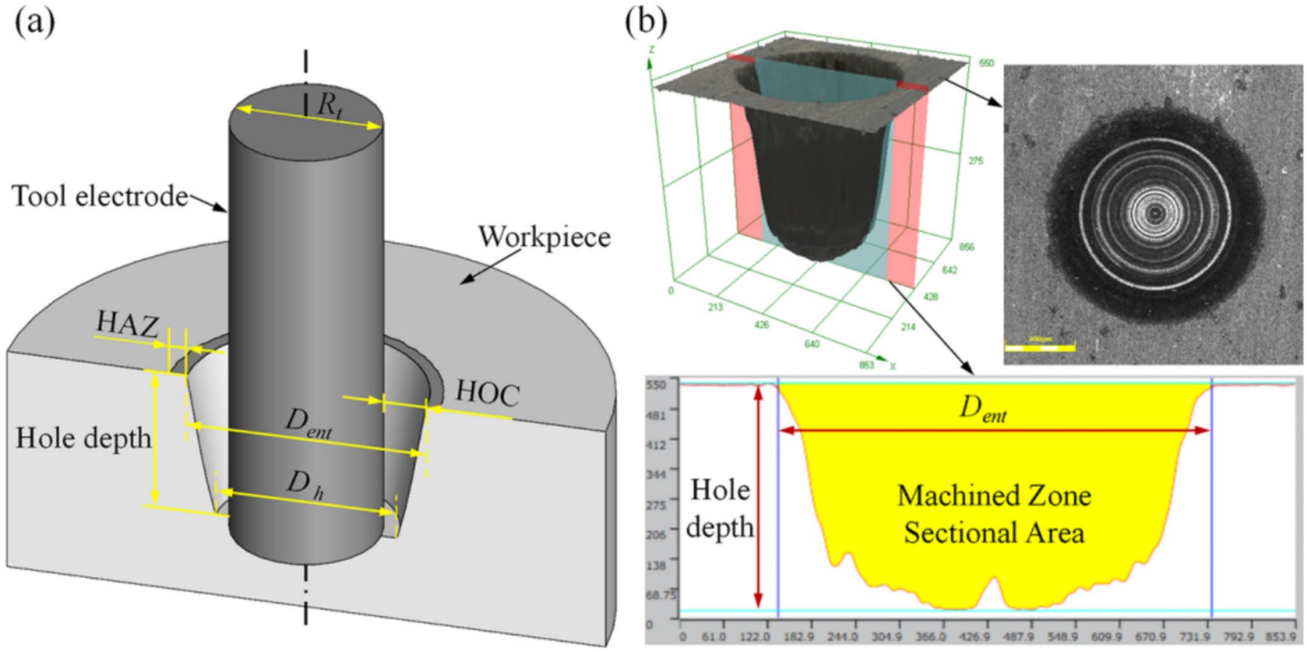

Fig. 4 **a** Schematic diagrams of the parameters of small hole and **b** 3D profile and section profile of the fabricated small hole

Table 3 Parameters of the high-speed camera experiment on gas films formation process

Parameters	Value
Pulse voltage (V)	45
Pulse frequency (kHz)	15
Pulse duty cycle (%)	80
Rotation speed (rpm)	8000
Electrolyte	15 wt% KOH
Electrode immersion depth (mm)	4
Frame capture speed (fps)	8000

600-mesh abrasive electrode were selected as the tool electrode. Other experimental conditions are shown in Table 3.

The captured images are shown in Fig. 5. When the pulsed power is turned on, hydrogen bubbles begin to form on the submerged surface of the electrode and gradually grow. At 0.5 ms, the volume of bubbles generated is small because the electrolysis reaction has just started. At 2 ms, due to the high-speed rotation of the electrode, obvious bubble detachment can already be observed on the surface of the conventional electrode, while the bubble on the surface of the abrasive electrode continues to grow. It is also clear that the 200-mesh abrasive electrode produces larger bubbles. At 4 ms, as more bubbles covering the entire submerged surface of the electrode, the bubbles accumulated on the surface of the conventional electrode have formed a distinct gas film. At this time, the bubbles on the surface of the abrasive electrode further increase and overflow into the electrolyte. The detachment radius of an overflowing bubble on the outer surface of the 200-mesh abrasive electrode was measured to be approximately 216 μm. At 12 ms, all three electrodes had formed gas film on the surface and wrapped around the tool electrodes. It can be observed that a thicker and unevenly distributed gas film is formed on the surface of the 200-mesh abrasive electrode, which is significantly different from the gas film formed by the conventional electrode and the 600-mesh abrasive electrode.

In the model developed by Jiang et al. [31], it was assumed that the gas bubbles attached to the surface of the tool electrode were uniformly distributed, and the total volume V of the gas produced and the average thickness δ of the gas film formed by the bubbles were estimated from the current during the electrolysis process:

$$\dot{V}(t) = \frac{i(t)R_g T}{ZFP} \tag{2}$$

$$i(t) = j(t)A \tag{3}$$

$$\delta = \frac{\int_0^{t_g} \dot{V}(t)dt}{A} = \int_0^{t_g} \frac{j(t)R_g T}{ZFP}dt \tag{4}$$

where V is the total volume of gas produced by electrolysis, i is the current of the electrolysis process, j is the current density, R_g is the gas constant, T is the temperature of gas, Z is the number of valencies changed in the gas generation reaction, F is Faraday's constant, P is the gas pressure, A is

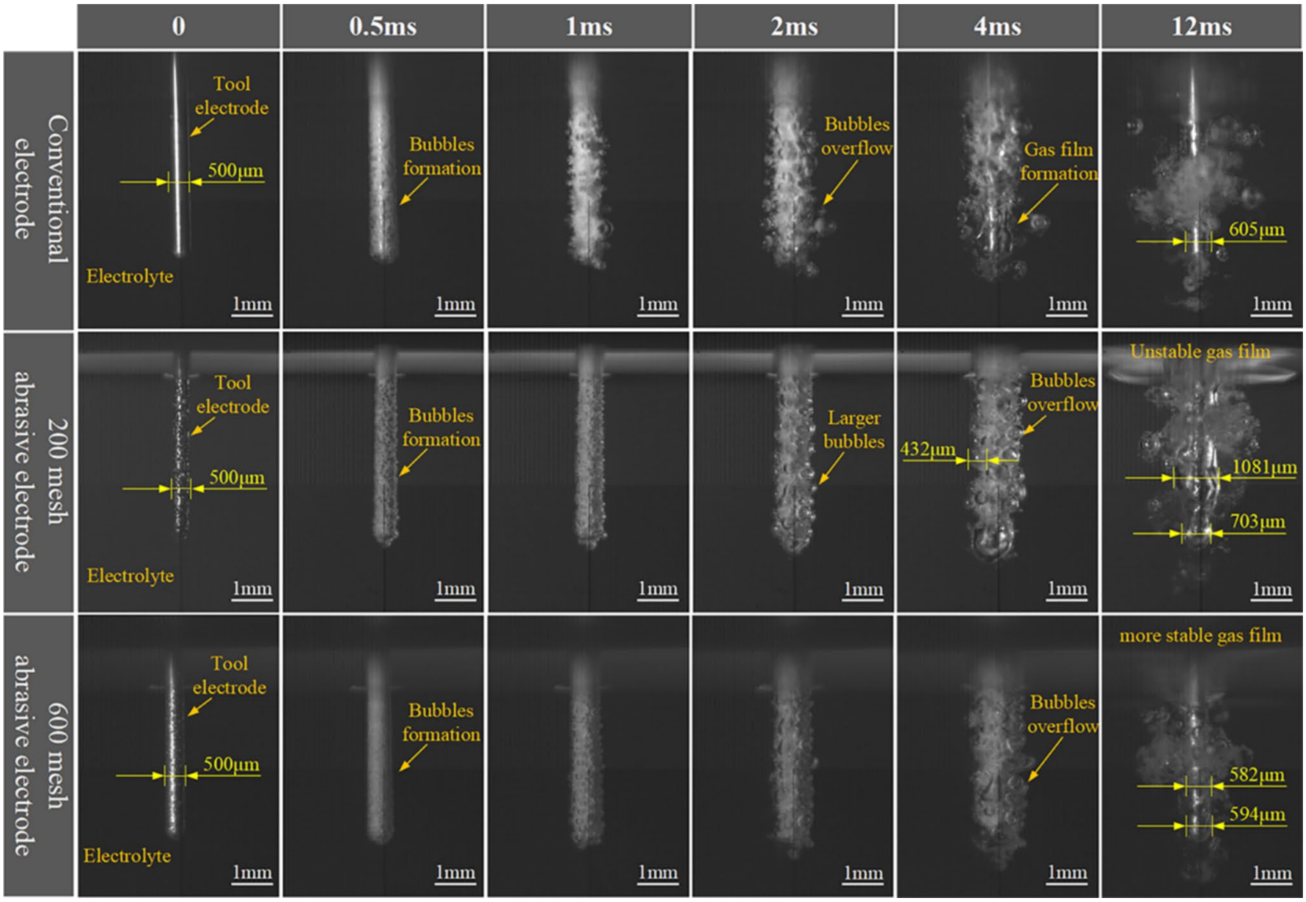

Fig. 5 Formation of gas film on the surface of different tool electrodes

the effective contact area between the tool electrodes and the electrolyte, and t_g is the time for the bubbles to detach from the tool electrodes.

As shown in Eq. 3, when the current is constant, the insulating diamond coated on the surface of the abrasive grain electrode reduces the effective contact area between the tool electrode and the electrolyte. Bubble nucleation occurs only on the surface of the electrically conductive electrode substrate, resulting in an increased current density. The rate of gas bubble generation is accelerated, and from this perspective, abrasive electrodes are more favorable for faster gas film formation. However, as shown in Fig. 5, as a large number of diamond abrasive grains coated on the surface of the tool electrode increase its surface roughness compared to the untreated cylindrical electrode, which will affect the bubble growth. In the report of Yang et al. [32], this phenomenon was explained using the Wenzel model: the rough surface of the tool electrode exhibits poorer wettability, and the surface tension of the bubbles adhering to the poorly wettable electrode is enhanced, which in turn leads to a thicker gas film.

Especially for larger size abrasive, the gap between adjacent abrasive particles and the electrode substrate forms a micro-cavity, providing more space for the growth of gas bubbles and prolongs the attachment time of the gas bubbles, resulting in the generation of a thicker gas film. However, for small sized abrasive, the protruding height of the abrasive grains on the electrode surface is not significant, and the micro-cavity established between the abrasive grains and the substrate has a weaker retention capacity for bubbles.

4 Exploration of the mechanism of G-ECDM of ZrO_2

4.1 Material properties of ZrO_2

The thermophysical properties of the zirconia ceramic materials used for the workpieces were provided by the manufacturer, as shown in Table 4. Zirconia is known to have three different polycrystalline forms. The transformation between them is mainly affected by temperature, dopant

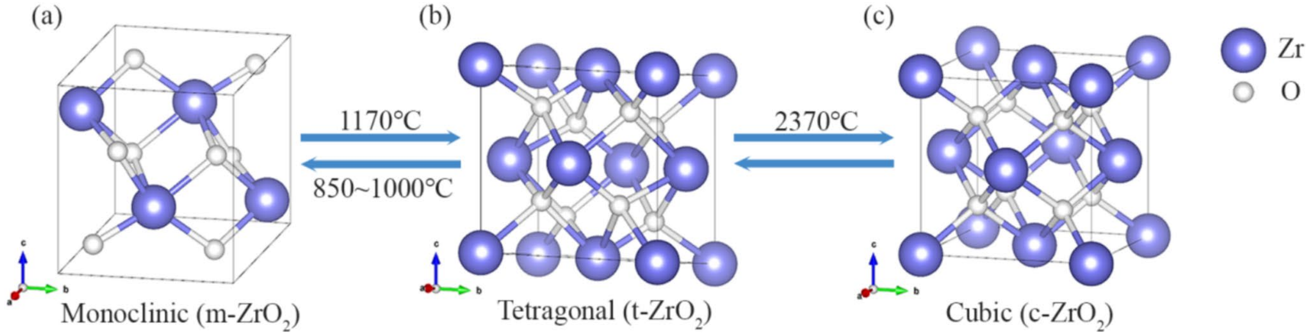

Fig. 6 Ball-and-stick model of the three structural phase of ZrO_2: **a** monoclinic, **b** tetragonal, and **c** cubic

Table 4 ZrO_2 ceramic thermophysical properties

Density	Specific heat capacity	Thermal conductivity	Melting point
ρ(kg m^{-3})	C_p(J kg^{-1} K^{-1})	k_w (W m^{-1} K^{-1})	T_m (K)
5850	400	3	2973.15

and mechanical loading [33]. As shown in Fig. 6, zirconia exists as a monoclinic phase (m-ZrO_2) at room temperature, which transforms into tetragonal phase (t-ZrO_2) when the temperature gradually increased up to about 1170 °C. When the temperature is further increased to about 2370 °C, it transforms into cubic phase (c-ZrO2). The solid-ZrO_2 begins to melt and transforms into liquid-ZrO_2 when the temperature is increased to 2715 °C. These phase transitions occur with a certain degree of hysteresis, and the entire phase transition is reversible. During heating, the material undergoes a volume shrinkage of 5% during the transition from m-ZrO_2 to t-ZrO_2. Conversely, when cooled, the t-ZrO_2 to m-ZrO_2 transition is the martensitic phase transition, which produces an expansion of 3–4% accompanied by a shear strain of about 8% [29].

4.2 Material removal mechanism of G-ECDM of ZrO_2 ceramics

Exploring the processing mechanism is essential for improving the processing efficiency and control the processing quality. However, the current research on the processing mechanism mainly focuses on glass materials, and there is some controversy regarding the removal mechanism of ceramic materials such as ZrO_2. He et al. [34] compared the concentration of Zr ion in the processed electrolyte with that in the electrolyte only soaked with ZrO_2, and found that the Zr ions concentration in the former was close to saturation. In addition, the detailed phase composition of the processed debris was analyzed by Raman spectroscopy. It is considered that the black debris produced during processing is the supersaturated precipitation of Zr ions to form amorphous ZrO_2 (a-ZrO_2), while the other white debris is produced by thermal exfoliation and high temperature melting. In contrast, in the report of Singh et al. [35], only the traces of ceramic thermal exfoliation and high temperature melting were observed on the machined surface, but the EDS analysis showed that the elemental composition of the material surface remained unchanged before and after processing. Therefore, it is considered that the material is almost not subjected to chemical etching at high temperatures during processing. There is consensus that the physical removal of ZrO_2 in ECDM is due to the instantaneous high temperature generated by the discharge and the material spalling caused by the internal stress [6].

Figure 7 shows a comparison of schematic diagrams and processing examples for the ECDM and G-ECDM processes. When machining ZrO_2 ceramics with conventional ECDM, the local surface temperature of the workpiece increases rapidly due to the high temperature of the spark discharge, generating significant thermal stress within the material. This results in the formation of micro-cracks on the surface of the workpiece. As the temperature continues to rise and the heat accumulates, the micro-cracks expand and extend beyond the target machining area, leading to a larger hole diameter and taper, or even fracture of the ceramic workpiece. The introduction of grinding action can remove the crack-producing material more quickly and avoid excessive heat accumulation inside the material. It is worth noting that in force-feed conventional ECDM, the working gap is extremely small, making it difficult to form a gas film at the tip of the electrode, which usually leaves a tab of certain height in the center of the hole. However, in G-ECDM, the abrasive grains at the electrode end provide micro cavities as nucleation sites for bubble growth at the bottom of the small hole. The bubbles will form thin and stable gas film in these micro cavities, which will not only eliminate the bumps, but will also result in greater machining depth [36].

As shown in Fig. 8 and Fig. 9, the surface characteristics at the bottom of small holes machined by ECDM and

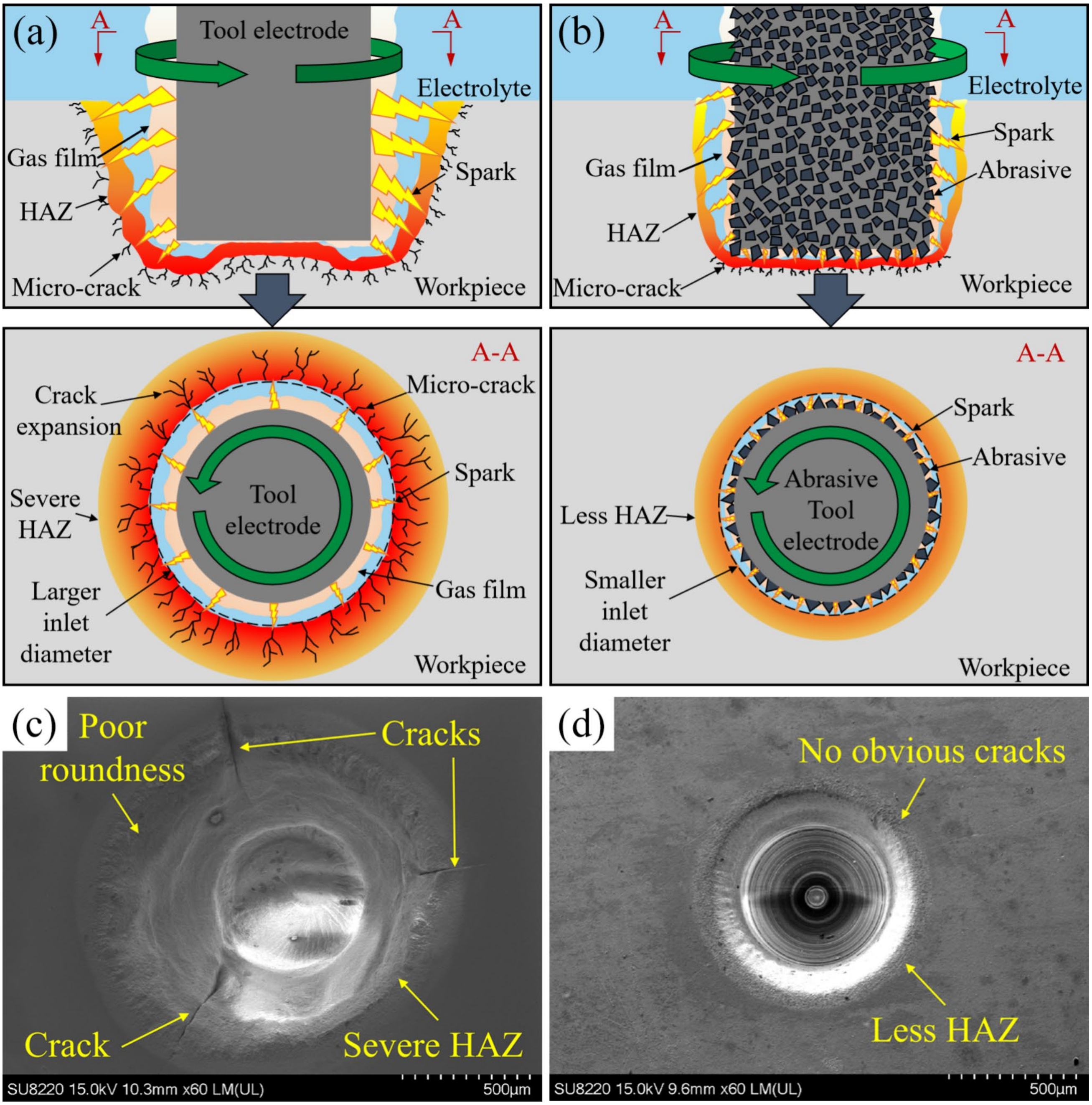

Fig. 7 Comparison of ECDM and G-ECDM processes: schematic diagrams of **a** ECDM and **b** G-ECDM processes, and examples of small holes machined by **c** ECDM and **d** G-ECDM

G-ECDM under the same conditions are compared. In the surface morphology of small holes processed by ECDM, fracture cracks are mainly generated along the grain gaps or grain boundary interfaces. The shape and size of the grains can be clearly seen, with a single grain size of about 0.6 μm, and obvious craters and holes formed as a result of the grains pull-out, which is characteristic of intergranular fracture damage (Fig. 8b). According to the analysis of the thermal spall removal mechanism of ZrO_2 ceramics by Singh et al. [35], when large thermal stresses are generated within the material, cracks are more likely propagate along grain boundaries due to the larger stress concentrations at the boundaries of the ZrO_2 grains. As shown in Fig. 8c, traces of partial melting were also found on the machined surface. As observed in Fig. 9a, there is a clear difference between the indicated area '1' and area '2' on the G-ECDM surface. The main reasons for the co-existence of these two fracture damage regions on G-ECDM surfaces are

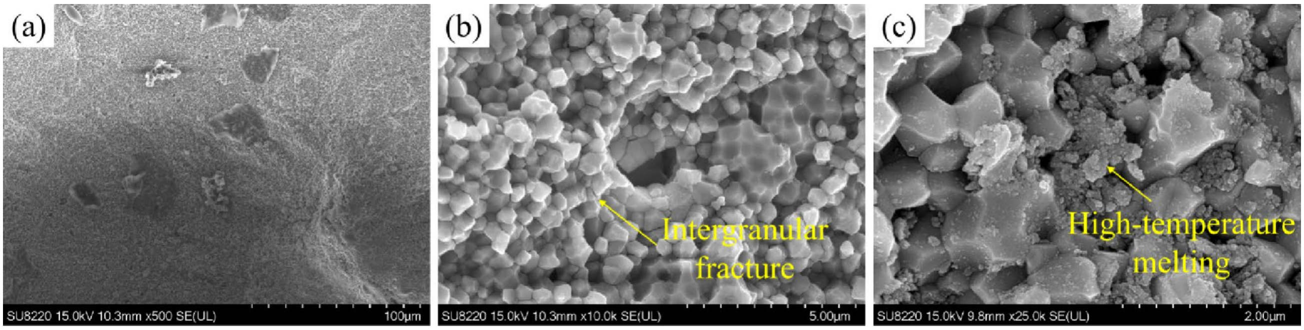

Fig. 8 SEM images of the surface of small holes in ZrO_2 ceramics machined by ECDM. **a** Small hole bottom surface. **b** Localized magnification image. **c** High-temperature melting traces

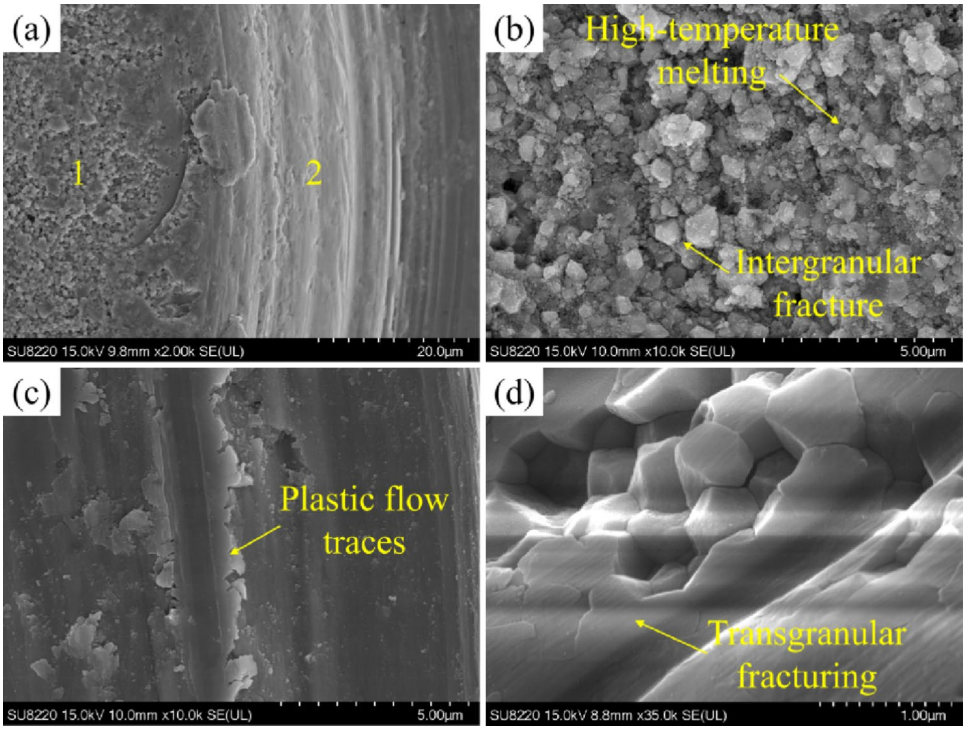

Fig. 9 SEM images of the surface of small holes in zirconia ceramics machined by G-ECDM. **a** Small hole bottom surface. **b** Localized enlarged image in area ‘1’. **c** Localized enlarged image in area ‘2’. **d** Transgranular fracture in area ‘2’

the random distribution of abrasive particles on the tool, differences in isotropy, and localized abrasive grain shedding. In area ‘1’, fracture cracks are generated along grain gaps or grain boundary interfaces, where damage is manifested as intergranular fracture. In area ‘2’, abrasive grits grind grooves leaving raised material on both sides, and no visible microcracks are present in the vicinity. As in Fig. 9d, a flat grain section and no obvious grain shape contours are also observed in area ‘2’, which corresponds to perforation fracture damage. Obviously, this smooth plastic removal is more conducive to higher surface quality than the brittle removal by intergranular fracture in ECDM.

Figure 10 shows the EDS results of the surface before and after machining. The main components of the unprocessed surface are Zr, O, and Y elements, which account for about 67.76%, 29.33%, and 2.90% by weight, respectively. On the machined surface, the content of Zr element was significantly reduced, while the content of O element was increased. The K element in the KOH electrolyte was not detected on the surface. The introduction of about 18.41% C is attributed to the graphitization of diamond grit tips at high temperatures during machining, and the graphitized portion of the grits can easily wear off and remain on the workpiece surface.

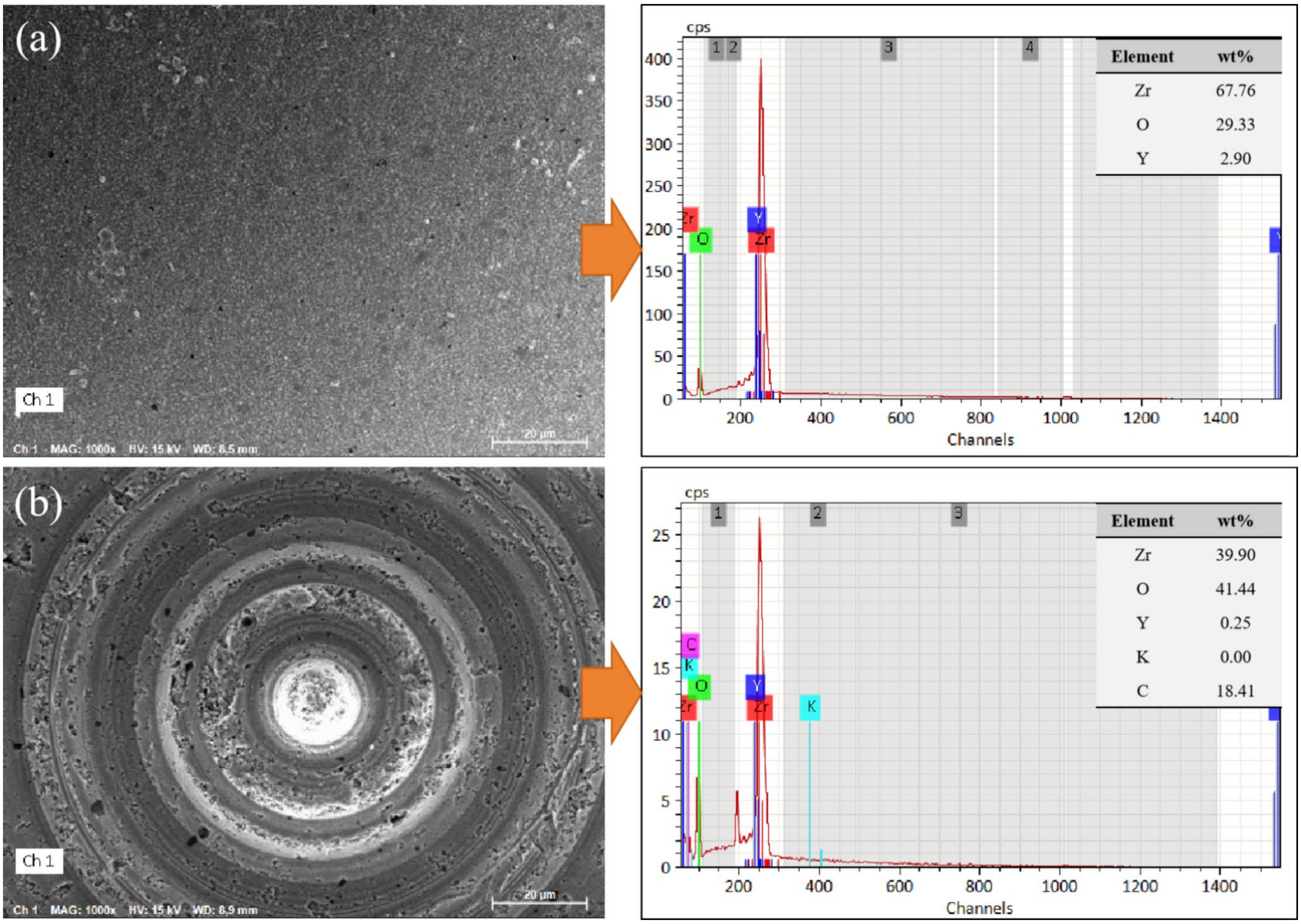

Element	wt%
Zr	67.76
O	29.33
Y	2.90

Element	wt%
Zr	39.90
O	41.44
Y	0.25
K	0.00
C	18.41

Fig. 10 EDS analysis of **a** un-machined surface and **b** machined surface by G-ECDM

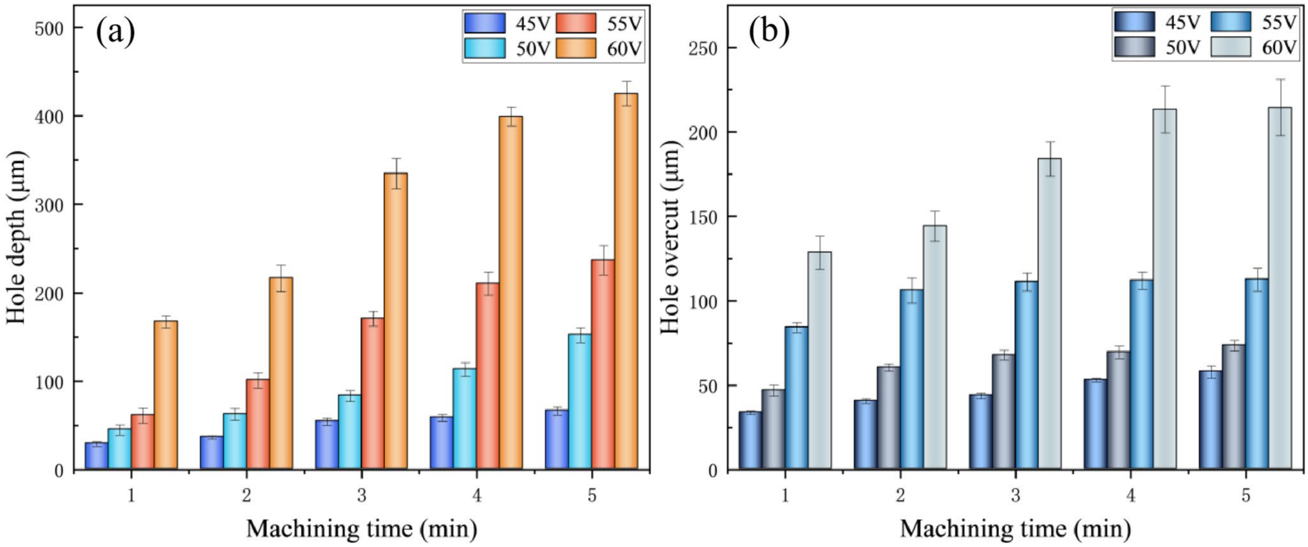

Fig. 11 Effect of voltage on the hole depth and the overcut of small holes: **a** hole depth, **b** hole overcut

5 Experiment and analysis

5.1 Effect of voltage on the small hole formation

The applied voltage directly affects the total thermal energy generated during ECDM. This is due to the fact that a higher voltage accelerates the electrolytic reaction, generates more hydrogen bubbles at the tool electrode, results in a higher frequency of spark discharges, and increases the amount of energy released per spark. This leads to higher MRR and a larger hole entry diameter. The hole depth and HOC of small holes machined at different voltages for durations ranging from 1 to 5 min were measured, and the results are shown in Fig. 11. For example, at 5 min, when the voltage was increased from 45 to 60 V, the HOC increased from 57.9 to 214 µm, and the machining depth increased from 66.4 to 425.2 µm. As the machining time increases, the HOC gradually increases and stabilizes due to the continuous influence of the electrochemical discharge at the entrance of the hole. With increasing machining depth, the circulation of electrolyte in the hole becomes difficult, which reduces the frequency of spark discharge at the extreme end of the electrode, and thus the growth rate of machining depth gradually decreases. Moreover, as shown in Fig. 12, the machining result at the initial stage exhibits a ring-like structure with a pit profile and a material residue in the center of the target machining area. This occurs because during the early machining phase, the electric field strength at the edge of the electrode end is higher, and the electrolyte supply is more abundant compared to the central region, leading to more concentrated discharge. As machining progresses, the gradually enlarging annular pits draw more electrolyte into the electrode tip, causing the discharge point to shift toward the center of the electrode end, thereby removing residual material from center of the hole [37]. Furthermore, as the applied voltage increases, the discharge energy and end discharge frequency also increase, causing the discharge point to move more rapidly toward the center region, and allowing the electrode to machine downward more quickly.

Although a further increase in applied voltage may increase the MRR, it may also increase the HAZ, which can lead to severe HOC and thermal damage. Meanwhile, the larger discharge energy will generate stronger thermal stresses inside the workpiece, resulting in more microcracks. The association and expansion of these cracks will weaken the material strength and may even cause fracture of the workpiece [38].

5.2 Effect of abrasive size on the small hole formation

As described in Fig. 5 above, different types of tool electrodes exhibit different gas film formation behavior during

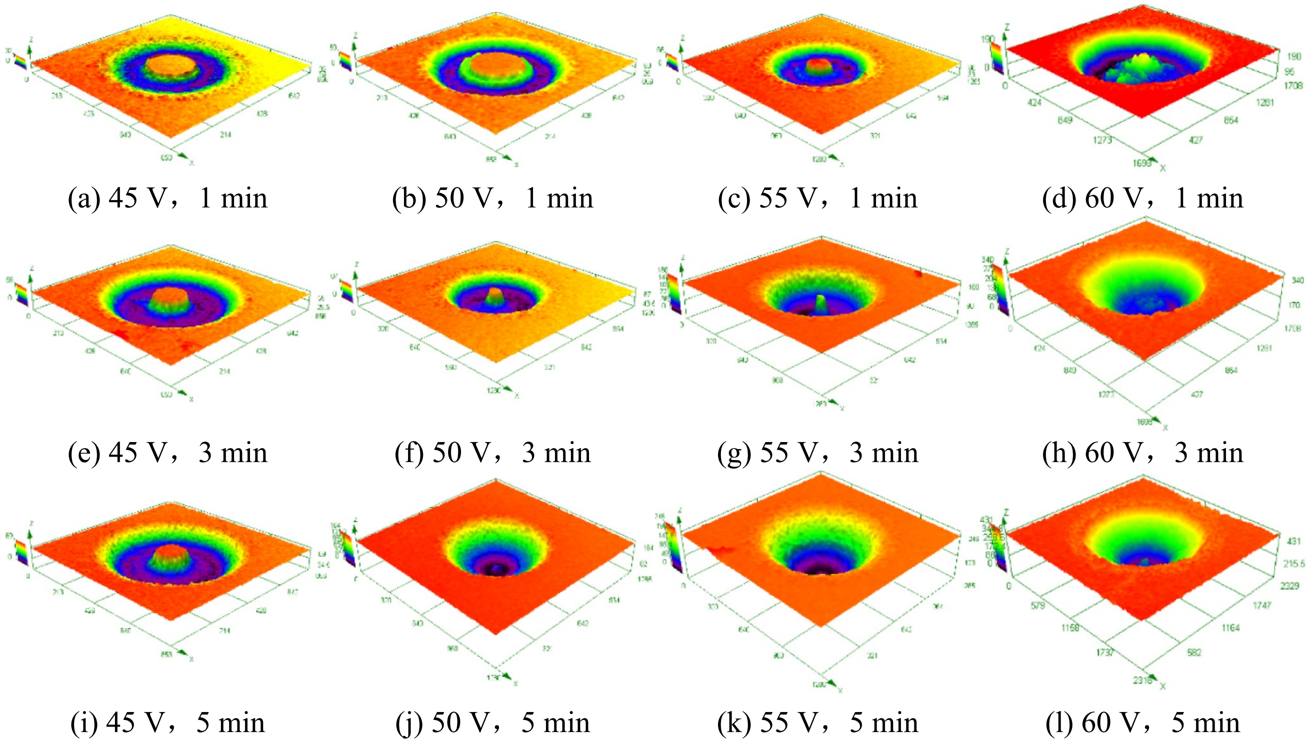
(a) 45 V，1 min (b) 50 V，1 min (c) 55 V，1 min (d) 60 V，1 min

(e) 45 V，3 min (f) 50 V，3 min (g) 55 V，3 min (h) 60 V，3 min

(i) 45 V，5 min (j) 50 V，5 min (k) 55 V，5 min (l) 60 V，5 min

Fig. 12 Three-dimensional profiles of small holes machined with different voltages

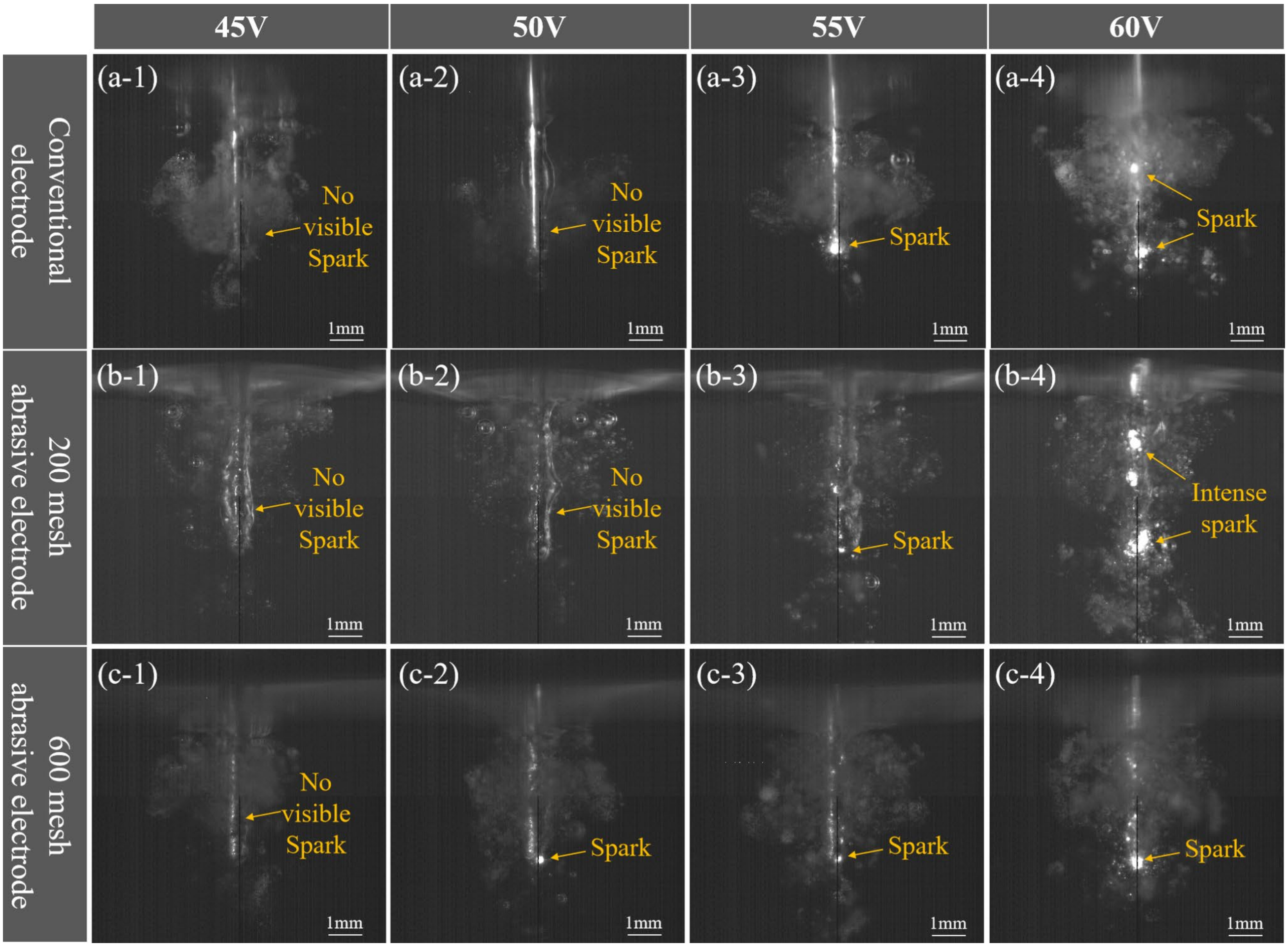

Fig. 13 The discharge conditions of different tool electrodes at different voltages

electrochemical discharge. And Fig. 13 shows the discharge conditions of different tool electrodes under different voltages. The frame capture time was 40 ms after energization, and the electrode speed and frame capture speed were set to 8000 rpm and 80,000 fps, respectively.

The captured image shows that the voltage required to discharge with the 600-mesh grit electrode is lower than that required for the other two electrodes. When the voltage was 60 V, the discharge area of both the 200-mesh abrasive grain electrode and the conventional electrode spread upward to the electrode sidewalls, where the 200-mesh abrasive grain electrode exhibited a more intense spark discharge. The spark discharge on the 600-mesh grit electrode appeared weaker than that of the other two electrodes, and the discharge point remained concentrated at the tip of the electrode. It is commonly recognized that spark discharge occurs when the applied voltage exceeds the breakdown critical voltage, and the magnitude of the breakdown critical voltage is mainly determined by factors such as the electrolyte, the geometry of the tool electrode [39]. For tool electrodes with a large number of insulating abrasive particles distributed on the surface, the conductive surface area is reduced, which decreases the difficulty of electrochemical discharge, and lowers the critical voltage.

Table 5 Comparison table of abrasive grains and sizes used in the G-ECDM experiments

Mesh number	200-mesh	400-mesh	600-mesh	800-mesh
Abrasive size	75 μm	38 μm	23 μm	18 μm

To further investigate the electrochemical discharge machining performance of conventional electrodes and electrodes with different abrasive grain mesh sizes, various types of electrodes were selected for the small-hole machining experiments. The voltage, frequency, and feed force were fixed at 60 V, 15 kHz, and 7 N, respectively. Table 5 shows the particle size of the different abrasive grains used in this study.

Figure 14 shows the machining results obtained using different electrodes under the same machining conditions. The

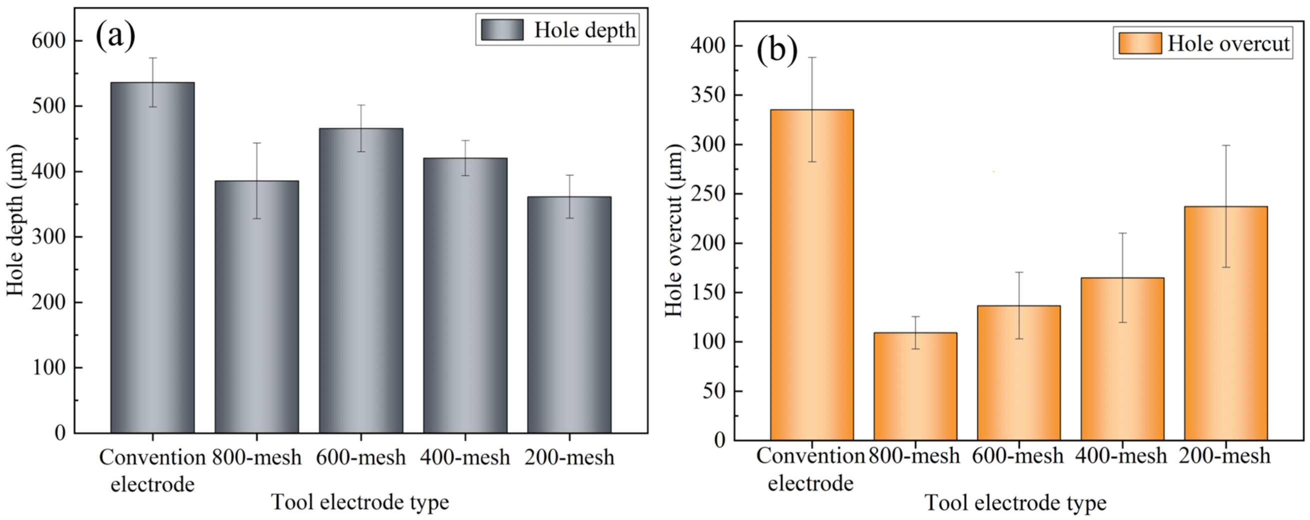

Fig. 14 Effect of abrasive grain size on the size of small holes: **a** hole depth, **b** hole overcut

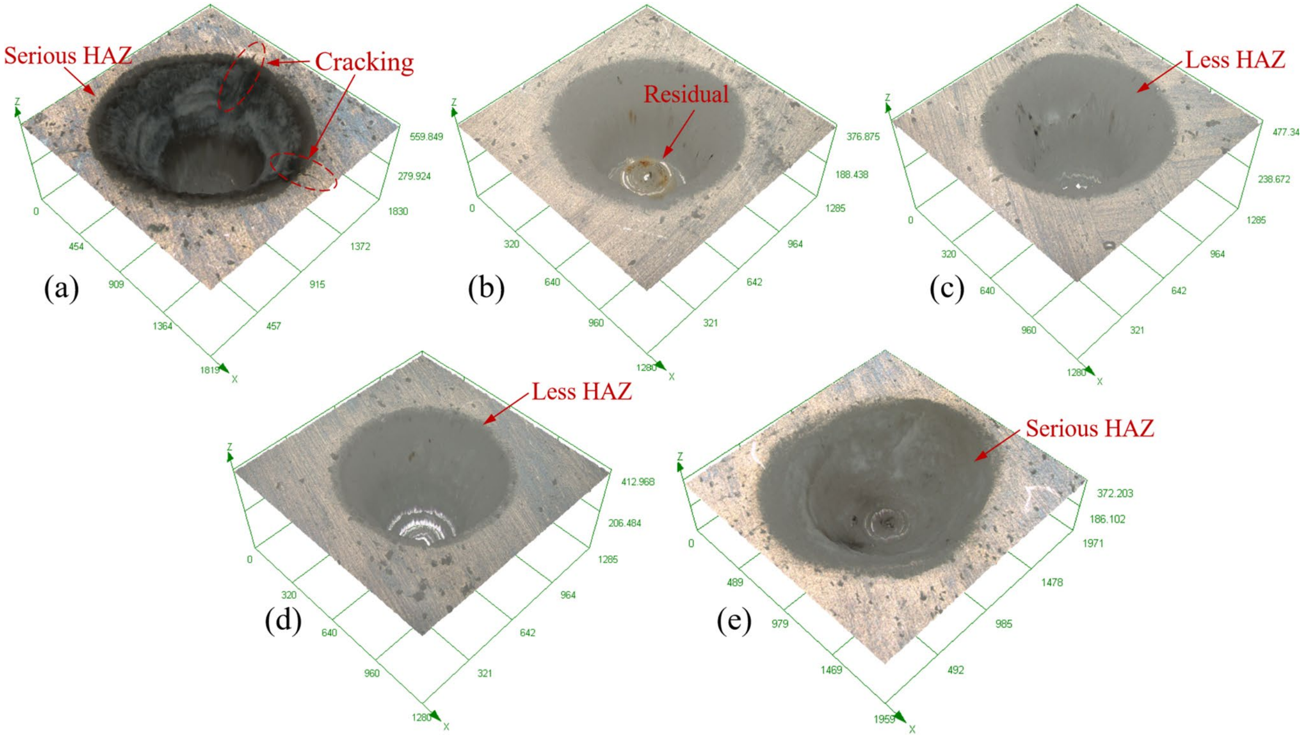

Fig. 15 Morphology of small holes machined by using different electrodes: **a** convention electrode, **b** 800-mesh abrasive electrode, **c** 600-mesh abrasive electrode, **d** 400-mesh abrasive electrode, **e** 200-mesh abrasive electrode

deepest small hole (559.8 μm) was obtained using conventional electrochemical discharge machining of ZrO_2, but its diameter was excessively large. Additionally, ablation marks on the wall surface of the small holes as well as several cracks can be clearly seen (Fig. 15a).

In G-ECDM, for the thicker and fluctuating gas film generated on the electrode surface with larger grain sizes (200-mesh) results in more intense and non-uniform electrochemical discharge energy, leading to severe HAZ and HOC. Moreover, the larger particle size results in a bigger gap between the electrode substrate and the surface of the workpiece, causing greater dissipation of the heat energy generated by the electrochemical discharge. In contrary, smaller abrasive particles reduce the gap between the electrode

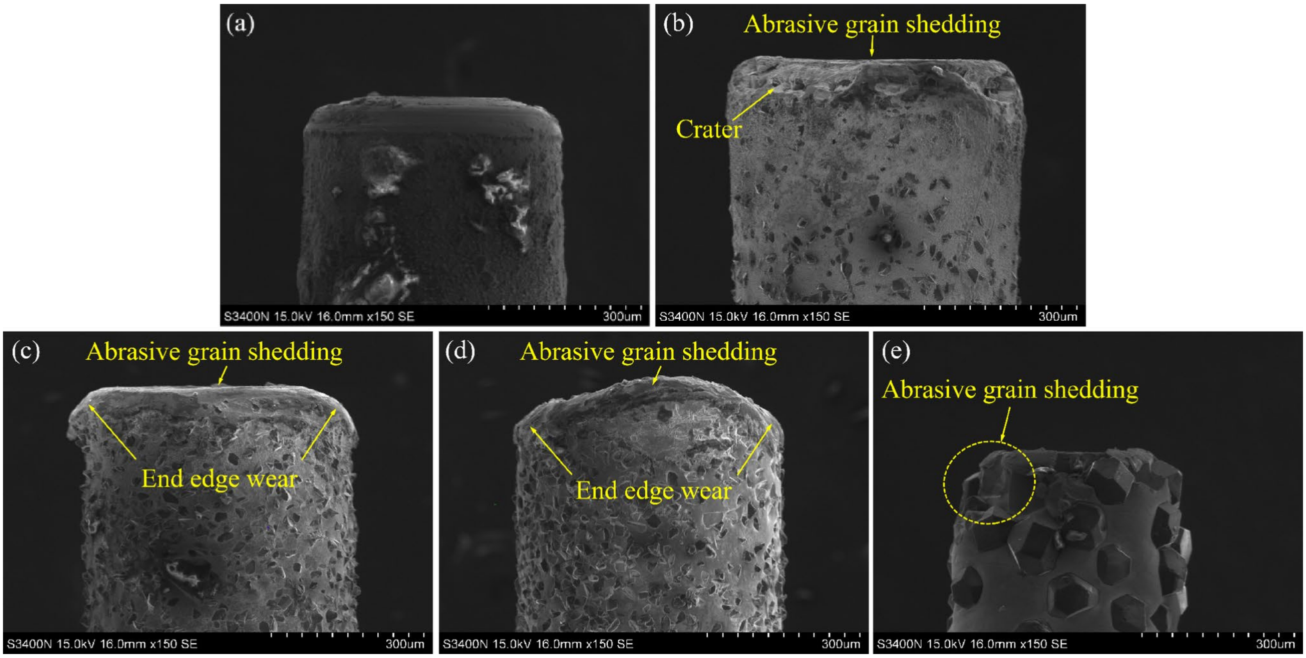

Fig. 16 Wear on different types of tool electrodes: **a** conventional electrode, **b** 800-mesh abrasive electrode, **c** 600-mesh abrasive electrode, **d** 400-mesh abrasive electrode, and **e** 200-mesh abrasive electrode

substrate and the workpiece surface, allowing more energy to be applied to material removal, which improves machining efficiency, and results in better machining accuracy.

In addition, as previously described, the gas film formed on the surface of the small size abrasive electrode is relatively thin and stable, which reduces stray discharge during processing. Hence the small holes produced have a smaller heat affected zone and HOC (Fig. 15c, d). However, if abrasive size is too small, the extremely narrow gap between the substrate material at the electrical tip and the workpiece makes it difficult for the electrolyte to enter, thus restricting the machining depth. For example, the 800-mesh abrasive electrode machined a hole depth of 376.8 µm and left a tab with a height of nearly 88.6 µm at the bottom center of the small hole (Fig. 15b). According to reference [40], the reason for the formation of the tab is that with a very small working gap, the discharge occurs more at the edge of the electrode, removing only the workpiece material in that vicinity.

Figure 16 compares the wear of different electrodes after machining. For the conventional electrode, because of direct contact with the workpiece, the discharge occurs more at the electrode edge and sidewall, so the electrode wear is more pronounced at these locations (Fig. 16a). On the small grain size abrasive electrode, the tool wear is mainly characterized by edge erosion and abrasive grain shedding at the ends (Fig. 16c, d). The difference is that some craters are observed at the end edge of the 800-mesh abrasive electrode (Fig. 16b). This may be because after some abrasive particles fall off the tool, an abrasive flow is formed at the end of the high-speed rotating tool, which constantly impacts both the workpiece and the tool, thus forming these defects. Larger grain sizes offer more resistance to the cutting edge of the abrasive grain during the grinding process, and the impact force generated by a single abrasive grain cutting the workpiece is greater. Therefore, the abrasive grains are more likely to shed and leave craters on the tool electrode (Fig. 16e). Taken together, the 600-mesh abrasive electrode showed better machining performance in the G-ECDM of ZrO_2 ceramics, and the same type of electrode was used in the subsequent experiments.

5.3 Effect of feed force on the small hole formation

The magnitude of the feed force has a direct influence on the grinding action in G-ECDM. It has also been reported that the gap between the tool electrode and the workpiece during machining can be controlled by applying different feed forces, which in turn affects the discharge removal effect on the workpiece [25]. In ECDM with constant force feed, the feed force is usually set to a low value of 1 to 2 N to avoid breakage, bending, and fragmentation of the workpiece material during machining of the finer tool electrodes [41]. For ZrO_2 ceramics, which have higher grinding resistance and higher hardness, this study attempts to machine them with higher feed forces to further improve the grinding action. The tool electrode used was a 600-mesh abrasive

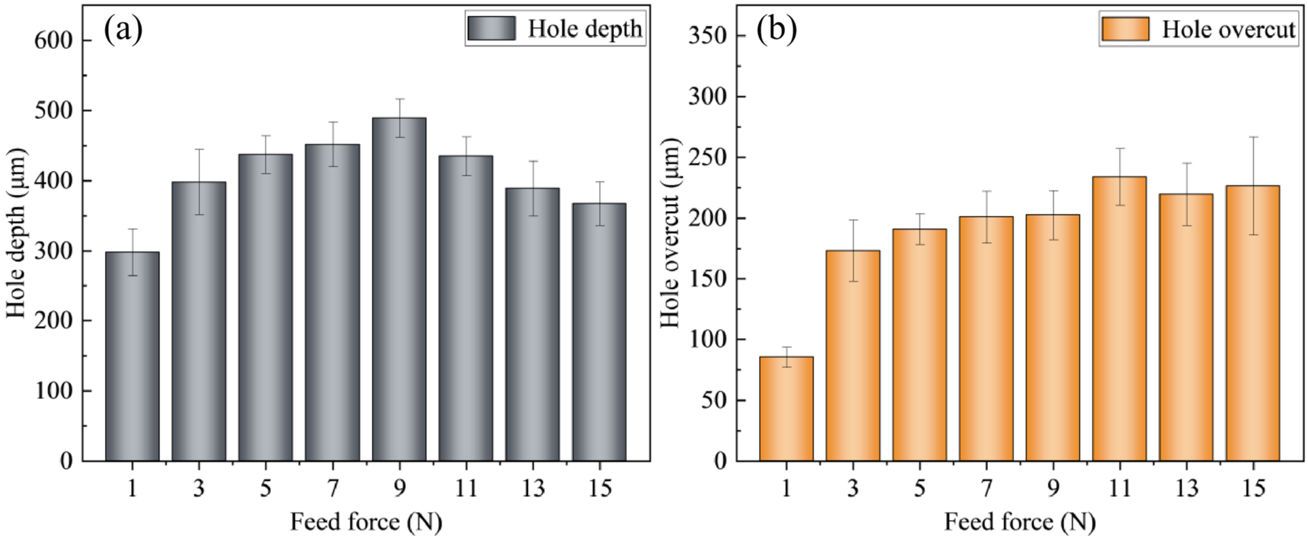

Fig. 17 The variation in hole depth and hole overcut with the feed force: **a** hole depth, **b** hole overcut

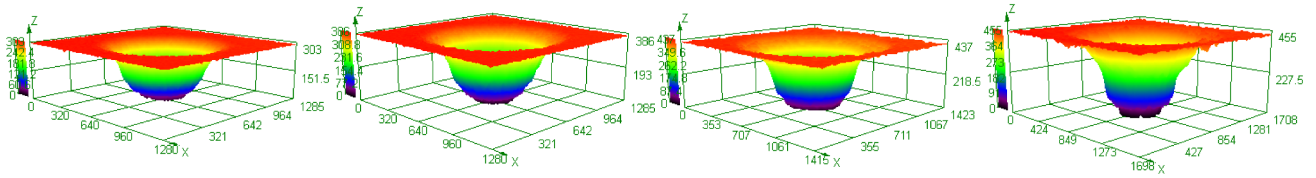

(a) 1 N (b) 3 N (c) 5 N (d) 7 N

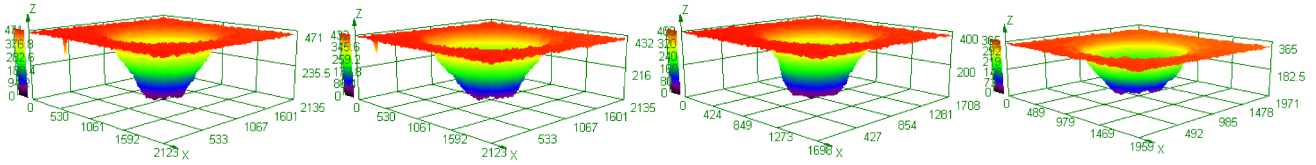

(e) 9 N (f) 11 N (g) 13 N (h) 15 N

Fig. 18 Effect of feed force on the size of small holes

electrode, and the voltage and frequency were set to 60 V and 15 kHz, respectively.

Figure 17 shows the hole depth and HOC machined at feed force from 1 to 15 N. Figure 18 illustrates the three-dimensional contours of these small holes. The machining depth initially increases and then decreases with increasing feed force, reaching a peak value of 489.4 μm at a feed force of 9 N. The amount of HOC increases from a minimum value of 85.3 μm at a feed force of 1 N to 173.2 μm at 3 N, and then increases slowly with further increase in feed force. The reasons for these outcomes are as follows: Lower feed forces reduce the grinding capacity of abrasive particles, directly affecting material removal. Conversely, the shear force experienced by the abrasive grains increases under a larger feed force, making the diamond abrasive grains more likely to crumble or fall off during the machining process. This significantly diminishes the abrasive effectiveness of the particles and also reduces the gap between the electrode base and the workpiece, thereby hindering electrolyte circulation and debris removal. Additionally, as shown in Fig. 19, under excessive feed force, the electrode tip undergoes severe extrusion deformation and bends upward along the gap between the hole and the electrode. At this point, the primary mechanism at the bottom of the hole is the mechanical grinding of the workpiece by the tool electrode substrate.

Figure 19 shows the tool wear at different feed forces. At smaller feed forces, no extrusion deformation was observed at the end of the tool electrode end (Fig. 19b). At a feed force of 9 N, most of the abrasive grains at the tip of the electrode have been shed, resulting in a flattened

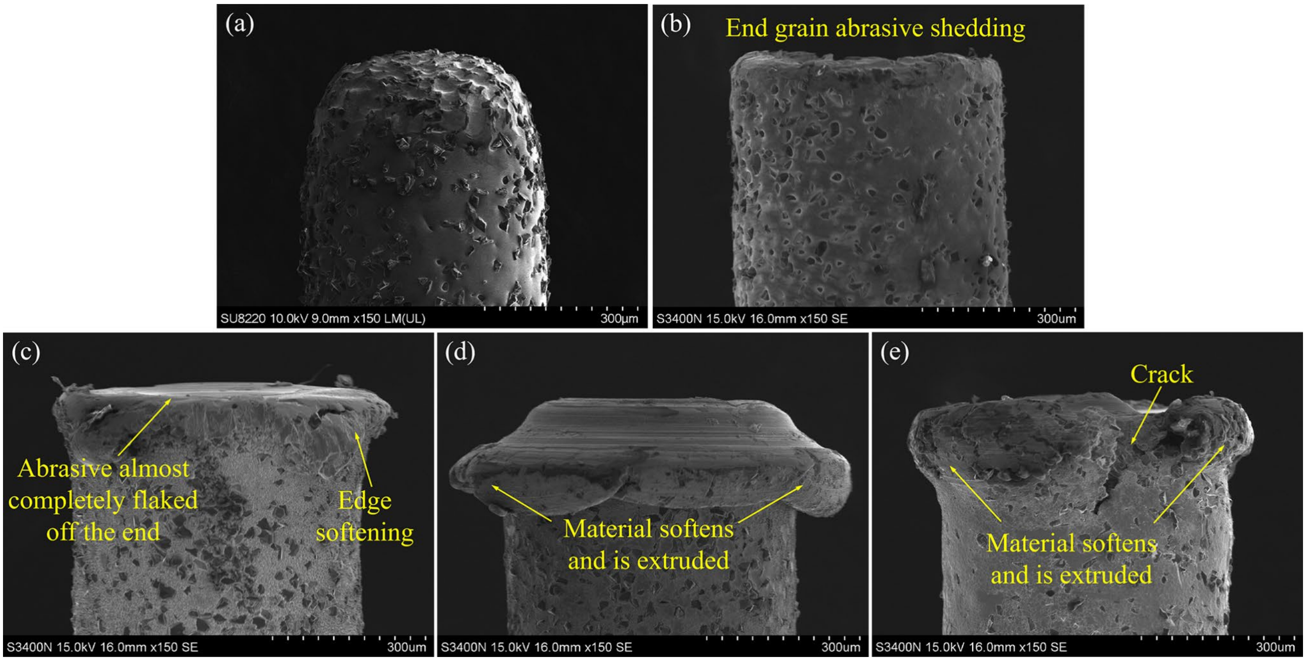

Fig. 19 Electrode wear at different feed forces: **a** before machining, **b** 5 N, **c** 9 N, **d** 13 N, and **e** 17 N

surface, while the end edges show obvious traces of melt softening (Fig. 19c). This melting and softening of the electrode substrate tip is especially noticeable at higher feed forces of 13 N and the softened tool material is deformed by the extrusion of the workpiece (Fig. 19d). This severe electrode wear not only increases the aperture diameter of the small holes but also makes further machining difficult. This is because the extruded material blocks the gap between the tool and the hole wall, hindering the inflow of electrolyte. At higher feed forces, the reduction in tool material strength at high temperature, combined with the increased grinding force, makes the tool more likely to break during machining (Fig. 19e).

5.4 Response surface optimization of parameter

To investigate the overall effect of G-ECDM process parameters on the machining performance of small holes of ZrO_2 ceramics, four factors, namely, voltage, frequency, speed, and feed force, were selected as input variables, denoted by A, B, C, and D, respectively. A CCD response surface analysis was carried out by using hole depth and HOC as output response indicators (Table 6). A 600-mesh abrasive electrode was selected as the tool.

The response values obtained from the experiments were analyzed using Design-Expert, and the quadratic fitting model was recommended for further analysis. According to the results of the analysis, for small hole depth, the significant degree of each factor is: Voltage > Frequency > Feed force > Rotation speed. For the amount of HOC, the order is: Voltage > Feed force > Frequency > Rotation speed. In both cases, the effect of voltage is extremely significant for both performance indicators. The regression equations for hole depth and HOC are given in Eqs. (5) and (6).

Table 6 Process parameters and their levels

Process parameter	Level 1	Level 2	Level 3
A: Voltage (V)	50	55	60
B: Frequency (Hz)	5000	10,000	15,000
C: Rotation speed (rpm)	4000	6000	8000
D: Feed force (N)	7	9	11
Y_1: Hole depth (μm)			
Y_2: HOC (μm)			

$$\begin{aligned} Y_1 &= 250.73 + 157.37 * A + 27.36 * B \\ &+ 16.72 * C + 23.04 * D + 17.31 * AD \\ &- 17.77 * CD + 66.11 * A^2 \end{aligned} \tag{5}$$

$$\begin{aligned} Y_2 =& 160.73 + 61.3 * \mathrm{A} - 14.17 * \mathrm{B} - 9.58 * \mathrm{C} + 20.72 * \mathrm{D} \\ &- 12.67 * \mathrm{AB} + 23.9 * \mathrm{AD} - 11.58 * \mathrm{CD} + 38.57 * \mathrm{A}^2 \\ &- 23.89 * \mathrm{C}^2 \end{aligned} \tag{6}$$

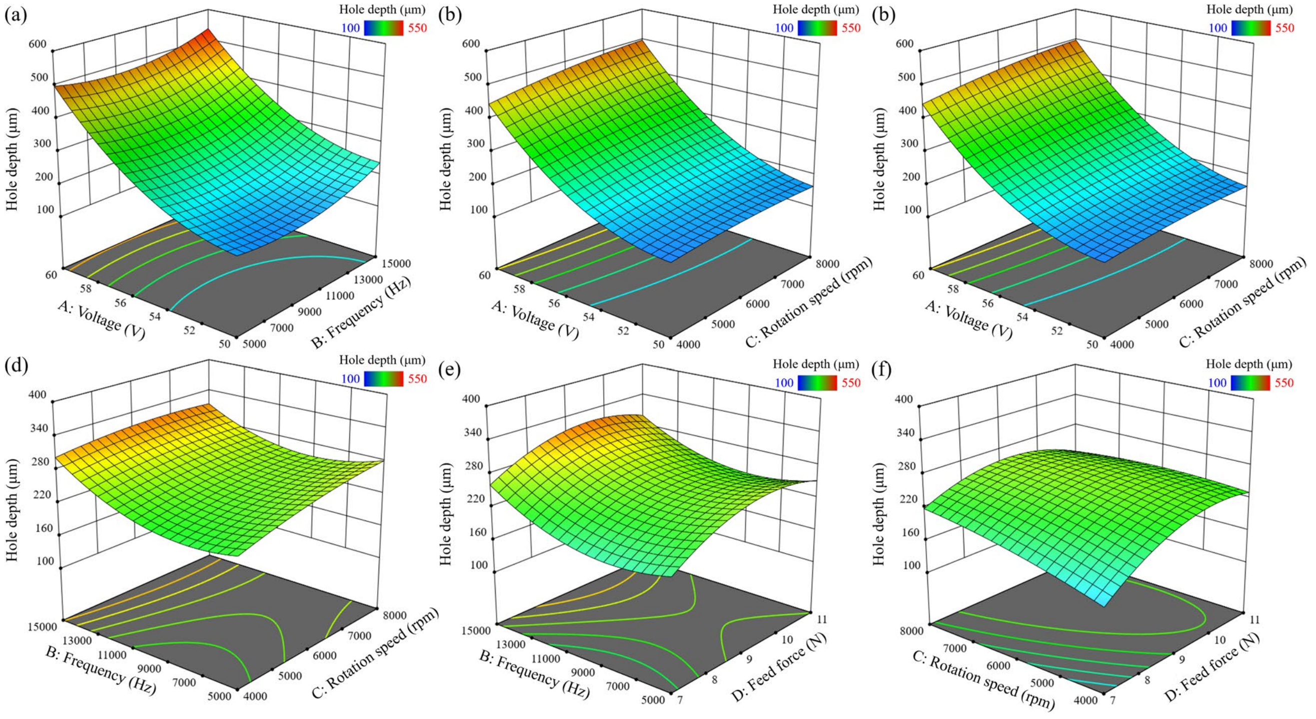

Fig. 20 3D response surface plots showing the effect of the interaction of factors (**A**: voltage, **B**: frequency, **C**: rotational speed and **D**: feed force) on the depth of small holes machined

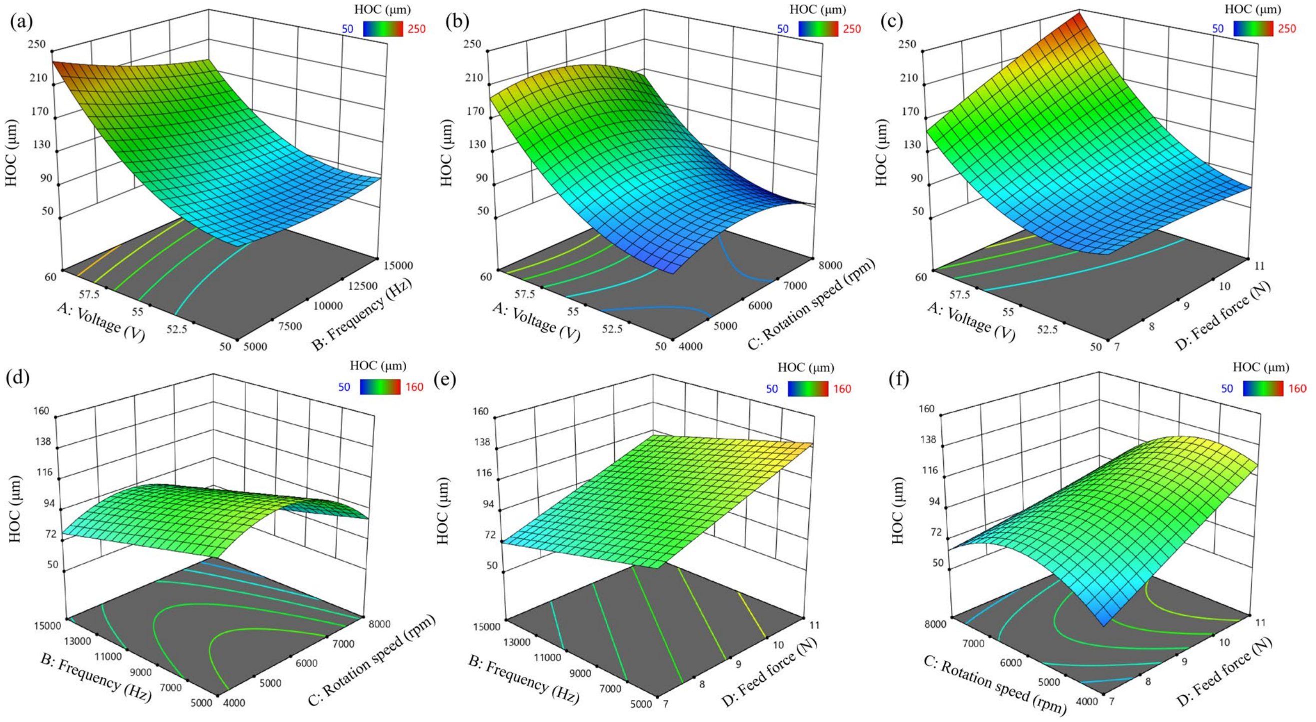

Fig. 21 3D response surface plots showing the effect of the interaction of factors (**A**: voltage, **B**: frequency, **C**: rotational speed and **D**: feed force) on the HOC of small holes machined

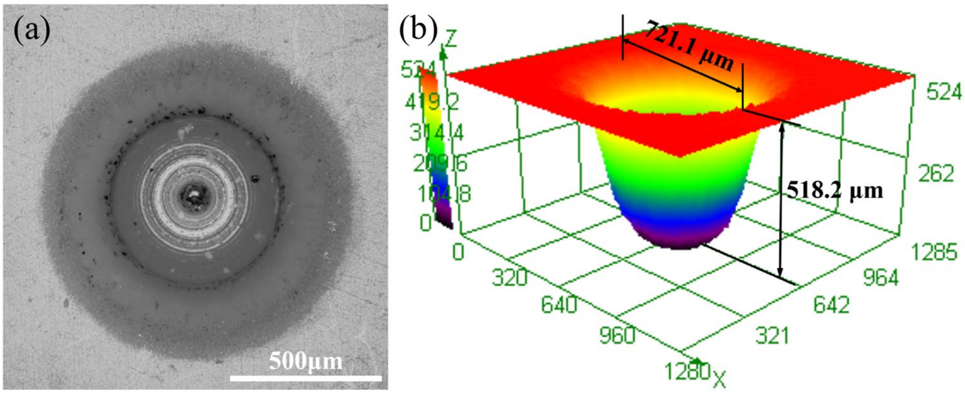

Fig. 22 Optimized machining results with optimal combination of parameters: **a** Surface morphology of small hole. **b** Three-dimensional contouring of small hole

Figures 20 and 21 exhibit the effect of the four processing variables on the output response in relation to each other. Voltage is the key parameter affecting both the area of influence and the energy of the electrochemical discharge. Lower voltages result in less heat fusion in the machined area, leading to lower grinding removal capability. As the voltage increases, the discharge energy also increase, enhancing the thermal fusion effect and reducing material strength, which improves the grinding removal capability.

The discharge duration increases with decreasing pulse frequency. For longer pulses, the heat generated by the discharge during a single pulse cycle increases significantly, leading to larger HAZ and HOC (Fig. 21a). Conversely, an increase in pulse frequency decreases the average energy of a single discharge, thus reducing the amount of material removed per discharge. However, in this experiment, the machining depth under high-frequency conditions was slightly increased (Fig. 20a). This may be due to the reduced degree of attrition of the abrasive electrode at high frequencies, which in turn improves the grinding action.

A combined increase in voltage and rotational speed, as well as voltage and feed force, were able to achieve greater hole depth (Fig. 20b, c). This indicates that the simultaneous enhancement of electrochemical discharge and grinding actions can improve the material removal capability. However, high applied voltages and high feed forces can lead to greater HOC (Fig. 21c), which is related to the electrode deformation mentioned earlier. Excessive deformation of the tool end causes discharge to occur more on the electrode sidewalls, resulting in greater HOC and thermal damage.

Increasing the rotational speed can improve the gas film stability and produce high frequency and low strength discharges. Moreover, the abrasive particles on the electrode surface can remove the cracked layer more quickly, avoiding heat accumulation and thus reducing the degree of thermal damage (Fig. 21b). At higher or lower combinations of feed force and rotation speed, severe tool wear greatly reduces the grinding action. When the working gap approaches zero, the discharge frequency at the tool end is also reduced, leading to a relatively shallow hole depth (Fig. 21f).

Furthermore, using the optimization module in Design Expert, equal weight optimization was performed using the maximum machining depth and HOC as the optimization objectives. The optimal parameter combinations were obtained as pulse voltage 60 V, frequency 15 kHz, electrode speed 8000 rpm, and feed force 7.5 N. When this combination of process parameters was applied, the resulting small holes are shown in Fig. 22. The depth of the small hole is 518.2 µm and the diameter is 721.1 µm, resulting in HOC of 110.5 µm. The edge of the hole is smooth, and there are no crack defects on its machined surface.

6 Conclusion

For ZrO_2 ceramics, traditional electrochemical discharge machining results in a large heat-affected zone, where thermal stress concentration can easily lead to microcracks, rupture and other issues. In this paper, a grinding-assisted electrochemical discharge machining process based on constant elasticity feedback feed is proposed, and the following conclusions were drawn from the study:

(1) The abrasive electrodes exhibit different gas film formation and discharge characteristics compared to conventional electrodes. Among them, the small size abrasive electrode facilitates the formation of a thin and stable gas film and produces a stable and low-intensity discharge, while the fluctuating and thicker gas film on the surface of larger-size abrasive electrode results in more violent discharge.

(2) The ability of G-ECDM to improve the machining quality and accuracy is demonstrated through small hole machining. It is also pointed out that the thermal spalling removal of ZrO_2 ceramics in ECDM is characterized by brittle removal dominated by intergranular

fracture damage, whereas in G-ECDM it is accompanied by transgranular fracture plastic deformation.

(3) Within the set parameter range, the hole overcut gradually increases with the abrasive grain size; however, the 600-mesh abrasive electrode demonstrates better performance.

(4) Within a certain range, increasing the feed force can increase the machining depth, but excessive feed force can lead to plastic deformation at the end of the electrode, hindering the supply of electrolyte in the machining area and negatively affecting the machining process.

(5) Through the dual-objective parameter optimization of hole depth and overcut, a set of optimal process parameters was obtained as follows: voltage 60 V, frequency 15 kHz, rotation speed 8000 rpm and feed force 7.5 N. Under these parameters, a hole depth of 518.2 μm and an of overcut of 110.55 μm were achieved.

Acknowledgements The work described in this paper was supported by a grant from the Research Grants Council of the Hong Kong Special Administrative Region, China (Project No. PolyU 15205323) and National Natural Science Foundation of China [grant numbers 52175387]. We are also thankful to the Guangdong University of Technology Analysis and Testing Center for LCSM, SEM and EDS support.

Author contributions Zhijian Huang: investigation, conceptualization, methodology, writing—original draft, writing—review and editing; Zhixiang Zou: methodology and writing—review; Zhiming Wu: investigation and measurement; Kangcheung Chan: formal analysis, writing—review, and editing; Jiangwen Liu: supervision, resources, writing—review, and editing.

Funding Open access funding provided by The Hong Kong Polytechnic University.

Declarations

Competing interests The authors declare no competing interests.

References

1. Yang R, Li KW, Yin LK, Ren K, Cheng Y, Li TT, Fu JP, Zhao TY, Chen ZG, Yang JL (2022) Study on the penetration power of ZrO2 toughened Al2O3 ceramic composite projectile into ceramic composite armor. Materials 15:2909. https://doi.org/10.3390/ma15082909
2. Guo M, Du J, Zhang Y (2024) ZrO2-reinforced polymer-matrix composites used for thermal protection systems of ultra-high temperature aerospace propulsion. Aerosp Sci Technol 145:108906. https://doi.org/10.1016/j.ast.2024.108906
3. Zhang F, Inokoshi M, Batuk M, Hadermann J, Naert I, Van Meerbeek B, Vieugels J (2016) Strength, toughness and aging stability of highly-translucent Y-TZP ceramics for dental restorations. Dent Mater Off Publ Acad Dent Mater 32:e327–e337. https://doi.org/10.1016/j.dental.2016.09.025
4. Vasudevan B, Natarajan Y, Sivalingam V, Krolczyk G, Tandon P (2022) Insights into drilling film cooling holes on ceramic-coated Nickel-based superalloys. Arch Civil Mech Eng 22:141. https://doi.org/10.1007/s43452-022-00465-x
5. Hsu HC, Wu SJ (2016) An investigation on micro-via drilling on ceramic substrates by a picosecond laser. In: 2016 IEEE 37th International Electronics Manufacturing Technology (IEMT) & 18th Electronics Materials and Packaging (EMAP) Conference. pp 1–4.
6. Bhattacharyya B, Doloi BN, Sorkhel SK (1999) Experimental investigations into electrochemical discharge machining (ECDM) of non-conductive ceramic materials. J Mater Process Technol 95:145–154. https://doi.org/10.1016/S0924-0136(99)00318-0
7. He JP, Cheng X, Zheng GM, Luo CZ, Li Y, Tang MZ (2024) Study on helical milling of small holes in zirconia ceramics with PCD tools. Int J Adv Manuf Technol 131:4773–4796. https://doi.org/10.1007/s00170-024-13295-3
8. Yang ZC, Zhu LD, Lin B, Zhang GX, Ni CB, Sui TY (2019) The grinding force modeling and experimental study of ZrO2 ceramic materials in ultrasonic vibration assisted grinding. Ceram Int 45:8873–8889. https://doi.org/10.1016/j.ceramint.2019.01.216
9. Wei CR, Zhang YM, Sugita N, Ito Y (2024) Generation mechanism and temporal–spatial evolution of electron excitation induced by an ultrashort pulse laser in zirconia ceramic. Appl Phys A 130:105. https://doi.org/10.1007/s00339-023-07223-7
10. Jagadish GK (2020) Abrasive water jet machining of ceramic composites. In: Gupta K (ed) Jagadish. Abrasive Water Jet Machining of Engineering Materials. Springer International Publishing, Cham, pp 51–71
11. Sabur A, Ali MY, Maleque MdA, Khan AA (2013) Investigation of material removal characteristics in EDM of nonconductive ZrO2 ceramic. Procedia Eng 56:696–701. https://doi.org/10.1016/j.proeng.2013.03.180
12. Ming WY, Jia HJ, Zhang HM, Zhang Z, Liu K, Du JG, Shen F, Zhang GJ (2020) A comprehensive review of electric discharge machining of advanced ceramics. Ceram Int 46:21813–21838. https://doi.org/10.1016/j.ceramint.2020.05.207
13. Fukuzawa Y, Mohri N, Tani T, Muttamara A (2004) Electrical discharge machining properties of noble crystals. J Mater Process Technol 149:393–397. https://doi.org/10.1016/j.jmatprotec.2003.12.028
14. Fukuzawa Y, Imata A, Kaneko Y, Harada T (2007) Mechanical strength of the wire EDMed insulating ZrO2 ceramics by assisting electrode method. In: Rajurkar KP, Resnick RL, Sundaram MM (eds) Proceedings of the 15th International Symposium on Electromachining. Univ Nebraska-Lincoln, Lincoln, pp 165–169
15. Jalali M, Maillard P, Wüthrich R (2009) Toward a better understanding of glass gravity-feed micro-hole drilling with electrochemical discharges. J Micromech Microeng 19:045001. https://doi.org/10.1088/0960-1317/19/4/045001
16. Wüthrich R, Hof L, Lal A, Fujisaki K, Bleuler H, Mandin P, Picard G (2005) Physical principles and miniaturization of spark assisted chemical engraving (SACE). J Micromech Microeng 15:S268. https://doi.org/10.1088/0960-1317/15/10/S03

17. Fascio V, Wuthrich R, Viquerat D, Langen H (1999) 3D microstructuring of glass using electrochemical discharge machining (ECDM). In: MHS'99. Proceedings of 1999 International Symposium on Micromechatronics and Human Science (Cat. No.99TH8478). pp 179–183
18. Arab J, Mishra DK, Dixit P (2021) Measurement and analysis of the geometric characteristics of microholes and tool wear for varying tool-workpiece gaps in electrochemical discharge drilling. Measurement 168:108463. https://doi.org/10.1016/j.measurement.2020.108463
19. Wüthrich R, Spaelter U, Wu Y, Bleuler H (2006) A systematic characterization method for gravity-feed micro-hole drilling in glass with spark assisted chemical engraving (SACE). J Micromech Microeng 16:1891. https://doi.org/10.1088/0960-1317/16/9/019
20. Xu Y, Chen JH, Jiang BY, Ni J (2018) Investigation of microdrilling using electrochemical discharge machining with counter resistant feeding. J Mater Process Technol 257:141–147. https://doi.org/10.1016/j.jmatprotec.2018.02.023
21. Abou Ziki JD, Wüthrich R (2013) Forces exerted on the tool-electrode during constant-feed glass micro-drilling by spark assisted chemical engraving. Int J Mach Tools Manuf 73:47–54. https://doi.org/10.1016/j.ijmachtools.2013.06.008
22. Tang WD, Zhu YH, Luo YQ, Mao C, Chen Y, Kang XM, Zhang MJ, Tang K, Zhang H, Zang A (2024) Detection of electrolyte supply state in the electrochemical discharge machining of micro hole based on deep learning. J Manuf Process 124:733–752. https://doi.org/10.1016/j.jmapro.2024.06.043
23. Nawaz SA, Cao P, Tong H, Li Y (2023) Micro ecdm scanning process with feedback control of flexible contact force. J Manuf Process 94:266–277. https://doi.org/10.1016/j.jmapro.2023.03.058
24. Nawaz SA, Cao P, Tong H, Li Y (2024) Micro ECDM process comparison using different tool feed methods of constant gravity and spring-force. J Phys Conf Ser 2671:012001. https://doi.org/10.1088/1742-6596/2671/1/012001
25. Singh T, Dvivedi A (2018) On pressurized feeding approach for effective control on working gap in ECDM. Mater Manuf Process 33:462–473. https://doi.org/10.1080/10426914.2017.1339319
26. Jain VK, Choudhury SK, Ramesh KM (2002) On the machining of alumina and glass. Int J Mach Tools Manuf 42:1269–1276. https://doi.org/10.1016/S0032-3861(02)00241-0
27. Wang TB, Liu Y, Wang K, Lv Z (2023) Investigation on a sustainable composite method of glass microstructures fabrication—electrochemical discharge milling and grinding (ECDM-G). J Clean Prod 387:135788. https://doi.org/10.1016/j.jclepro.2022.135788
28. Ladeesh VG, Manu R (2021) Grinding aided electrochemical discharge drilling (G-ECDD): a theoretical analysis and mathematical modelling of material removal rate. J Braz Soc Mech Sci Eng 43:422. https://doi.org/10.1007/s40430-021-03131-0
29. Xu S, Yao ZQ, Cai HY, Wang HY (2017) An experimental investigation of grinding force and energy in laser thermal shock-assisted grinding of zirconia ceramics. Int J Adv Manuf Technol 91:3299–3306. https://doi.org/10.1007/s00170-017-0013-y
30. Kumar N, Mandal N, Das AK (2020) Micro-machining through electrochemical discharge processes: a review. Mater Manuf Process 35:363–404. https://doi.org/10.1080/10426914.2020.1711922
31. Jiang BY, Lan SH, Wilt K, Ni J (2015) Modeling and experimental investigation of gas film in micro-electrochemical discharge machining process. Int J Mach Tools Manuf 90:8–15. https://doi.org/10.1016/j.ijmachtools.2014.11.006
32. Yang CK, Cheng CP, Mai CC, Wang AC, Hung JC, Yan BH (2010) Effect of surface roughness of tool electrode materials in ECDM performance. Int J Mach Tools Manuf 50:1088–1096. https://doi.org/10.1016/j.ijmachtools.2010.08.006
33. Verdi C, Karsai F, Liu P, Jinnouchi R, Kresse G (2021) Thermal transport and phase transitions of zirconia by on-the-fly machine-learned interatomic potentials. Npj Comput Mater 7:1–9. https://doi.org/10.1038/s41524-021-00630-5
34. He SQ, Tong H, Liu G (2018) Spark assisted chemical engraving (SACE) mechanism on ZrO2 ceramics by analyzing processed products. Ceram Int 44:7967–7971. https://doi.org/10.1016/j.ceramint.2018.01.236
35. Singh T, Dvivedi A (2021) Fabrication of micro holes in Yttria-stabilized zirconia (Y-SZ) by hybrid process of electrochemical discharge machining (ECDM). Ceram Int 47:23677–23681. https://doi.org/10.1016/j.ceramint.2021.05.017
36. Singh T, Dvivedi A (2018) On performance evaluation of textured tools during micro-channeling with ECDM. J Manuf Process 32:699–713. https://doi.org/10.1016/j.jmapro.2018.03.033
37. Kang XM, Tang WD, Zhao WS, Qian J, Lauwers B (2021) Experimental and numerical investigations of material removal process in electrochemical discharge machining of glass in discharge regime. Precis Eng 72:706–716. https://doi.org/10.1016/j.precisioneng.2021.07.014
38. Zhang YB, Gu HZ, Fu LP, Huang A, Zhang MJ (2023) Effect of pore structure and phase composition on thermal shock resistance of zirconia materials. Ceram Int 49:40120–40130. https://doi.org/10.1016/j.ceramint.2023.09.343
39. Wüthrich R, Fascio V (2005) Machining of non-conducting materials using electrochemical discharge phenomenon—an overview. Int J Mach Tools Manuf 45:1095–1108. https://doi.org/10.1016/j.ijmachtools.2004.11.011
40. Liu GD, Tong H, Wu TY, Li Y, Luo YG (2022) Chain discharging behavior induced by gas film expansion and its influence on the electrochemical discharge machining (ECDM) process. Int J Adv Manuf Technol 124:2755–2767. https://doi.org/10.1007/s00170-022-10665-7
41. Behroozfar A, Razfar MR (2016) Experimental study of the tool wear during the electrochemical discharge machining. Mater Manuf Process 31:574–580. https://doi.org/10.1080/10426914.2015.1004685